

ELECTRIC FIELD ENHANCEMENT OF PHOTOCATALYSIS

By

MICHAEL JOHN LAUDENSLAGER

A DISSERTATION PRESENTED TO THE GRADUATE SCHOOL
OF THE UNIVERSITY OF FLORIDA IN PARTIAL FULFILLMENT
OF THE REQUIREMENTS FOR THE DEGREE OF
DOCTOR OF PHILOSOPHY

UNIVERSITY OF FLORIDA

2013

© 2013 Michael John Laudenslager

ACKNOWLEDGMENTS

Pursuing a PhD cannot be accomplished alone. There are many people I want to thank that have helped me along the way. I am deeply grateful to have met and learned from each and everyone mentioned here as well as many others. First and foremost, I thank Dr. Sigmund, my research adviser. His continued guidance throughout the project has kept me on track, and his motivating personality has kept me excited about the projects I have worked on. I also extend my thanks to my committee members who have offered constructive criticism that has helped improve my dissertation.

Without the benefit of the several organizations that funded me, I would not have been able to put this dissertation together. I extend my thanks and gratitude to the people and organizations that have made this funding possible. Specifically, I'm thankful for the continued support from Sandia National labs and Dr. Nelson Bell. I'm also grateful for the financial assistance from the Alumni Fellowship from the University of Florida. For the chance to visit the beautiful country of South Korea and conduct research there, I thank the National Science Foundation East Asia and Pacific Islands Summer Institutes program (NSF-EAPSI 2010). I also thank my Korean research advisers and labmates from the Energy Engineering department at Hanyang University. I also extend my thanks to all of the graduate students I have worked with at UF. They have helped provide direction and their own perspectives and assistance in many areas of my research. Dr. Shu-Hau Hsu, Raymond Scheffler, Isaac Finger, Dr. Chris Woan, Dr. Hyoungjung Park, Dr. Palanikkumaran Muthiah, Dr. Apratim Biswas, Rui Qing, Emma Eggink, Aslıhan Süslü, Chris Bohling, and Nicole McFarland were all important to my development as a researcher. Finally, I would also like to show appreciate for the Major Analytical Instrumentation Center staff.

TABLE OF CONTENTS

	<u>page</u>
ACKNOWLEDGMENTS.....	3
LIST OF TABLES.....	6
LIST OF FIGURES.....	7
LIST OF ABBREVIATIONS.....	10
ABSTRACT.....	11
CHAPTER	
1 INTRODUCTION AND BACKGROUND.....	13
Photocatalysis.....	13
Surface Properties.....	15
TiO ₂ : Anatase, Rutile, and the P25 Standard.....	16
Methods to Improve Photocatalytic Performance.....	19
Photocatalyst Recovery.....	21
Photocatalytic Degradation of Dye Molecules.....	22
Reaction Kinetics.....	25
Parameters That Influence Photocatalytic Reaction Rates.....	26
Particle Size and Morphology Analysis.....	27
Zeta Potential.....	28
Electric Field Effects on Photocatalysts.....	29
Internal electric fields.....	29
External electric fields.....	30
Electric field effects on exciton separation.....	33
Sol-Gel Processing of Nanomaterials.....	35
Electrospinning of Nanofibers.....	36
Models of the Electrospinning Process.....	38
Ceramic Nanofibers.....	38
Salt Loaded Polymers.....	39
Electrospun Fiber Modifications.....	40
2 MATERIALS SYNTHESIS AND CHARACTERIZATION.....	49
Synthesis of Photocatalytic Materials.....	49
Material Characterization.....	50
3 ELECTRIC FIELD EFFECTS ON PHOTOCATALYTIC ACTIVITY.....	60
Introduction.....	60

Materials and Methods.....	60
UV-Vis Absorbance Calibration Curve.....	62
Solution Conductivity	63
Copper Electrode Photocatalytic System.....	63
Conclusions	64
Parallel Plate Electric Field Setup.....	64
Particle Motion in an Electric Field	65
Electric Field and UV Effect on Procion Red Dye.....	66
Electric Field Effects on a P25 Photocatalytic System	66
Electric Field Effects on Rutile, CNT/TiO ₂ , ZnO/TiO ₂	68
Photocatalytic Nanorods in an Electric Field	69
Conclusions	70
4 LIGHT INTERACTION WITH PHOTOCATALYTIC SYSTEMS	81
Introduction	81
Light Extinction through Dispersed Particles in Liquid	81
Conclusions	82
5 ELECTROSPINNING OF HIGH CONDUCTIVITY SOLUTIONS	86
Introduction	86
Materials and Methods.....	86
Solution Conductivity	87
Influence of Collector Shape.....	88
Fiber Diameter and Morphology	90
Applications	92
Conclusions	92
6 CONCLUSIONS AND FUTURE WORK	100
Conclusions	100
Future Work.....	101
LIST OF REFERENCES	102
BIOGRAPHICAL SKETCH.....	113

LIST OF TABLES

<u>Table</u>		<u>page</u>
1-1	Electron mobility in various forms of TiO ₂ materials.	44
2-1	Surface area predicted from Scherrer equation vs. BET measured surface area.	59
5-1	Conductivity of electrospinning solutions with varying amounts of NaCl addition on a circular collection plate with a diameter of 8.5 cm	94

LIST OF FIGURES

<u>Figure</u>	<u>page</u>
1-1 Band structure of a photocatalyst showing exciton generation in response to UV light.	42
1-2 Photocatalysis of Procion Red dye on mixed phase.....	42
1-3 Crystal structures of TiO ₂ showing the two most common phases.....	43
1-4 Band structures of anatase and rutile phases.....	44
1-5 Procion Red MX-5B dye molecule.....	45
1-6 Nanoparticle cluster being oriented and accelerated by an electric field.	45
1-7 Hydrolysis and subsequent condensation reaction of titanium methoxide.....	46
1-8 Diagram of a typical electrospinning apparatus.....	46
1-9 Timeline of the publication record on electrospun materials.	47
1-10 SEM images of as-spun electrospun TiO ₂ nanofibers at various stages during the annealing process.	48
2-1 X-ray diffraction of P25 and rutile nanoparticles.	54
2-2 XRD spectrum of CNT/TiO ₂ nanoparticles.....	54
2-3 XRD spectrum of ZnO/TiO ₂ nanoparticles. “A”, “R, and “Z” represent the anatase, rutile, and ZnO peaks, respectively.....	55
2-4 XRD of SrTiO ₃ : 20 % La electrospun nanorods.....	55
2-5 Grain size of photocatalytic materials reported from Scherrer equation.	56
2-6 BET surface area measurements of photocatalytic materials.....	56
2-7 SEM images taken at the same scale of (A) P25 (B) CNT/TiO ₂ , (C) rutile, and (D) ZnO/TiO ₂	57
2-8 TEM images of (A) P25 particles and (B) rutile particles.	58
2-9 SEM image of SrTiO ₃ :20 % La nanofibers after calcination.....	58
3-1 Absorbance curves of varying concentrations of Procion Red dye.....	71
3-2 Intensity vs. concentration of Procion Red dye.....	72

3-3	Electric field enhancement using copper electrodes.....	73
3-4	Types of photocatalytic reactors.....	73
3-5	Particle deposition on containers walls in an electric field.	74
3-6	Left: Rate constants of P25 in the presence of varying electric field strengths ...	75
3-7	Natural log of rate constant vs. square root of electric field strength.	76
3-8	Fitted equation based on Poole-Frenkel model.	77
3-9	Photocatalytic performance without an applied electric field and with an applied electric field of 2300 V/cm.	78
3-10	Photocatalytic performance without an applied electric field and with an applied electric field of 2300 V/cm normalized for surface area.....	79
3-11	Percentage improvement in k_{app} at 2300 V/cm over k_{app} without an applied electric field.....	80
3-12	Reaction rates of SrTiO ₃ with and without an applied electric field.....	80
4-1	Transmittance of varying quantities of P25 dispersed in DI water through a cuvette with an optical path length of 1 cm.....	84
4-2	Transmittance at 380 nm vs. P25 concentration in water.	85
5-1	0.01g NaCl resulted in fibers collecting as a flat mesh typically observed in electrospinning.	94
5-2	Photographs of electrospun fibers containing 0.05 g NaCl onto a collector with a diameter of 8.5 cm..	94
5-3	Photographs of electrospun fibers containing 0.1 g NaCl onto a collector with a diameter of 8.5 cm.....	95
5-4	Fiber collection with 0.05 g NaCl on a collector with a diameter of 5 cm	95
5-5	Conical strand of fibers extending outward from the collection plate (d=12 cm) towards the needle.	96
5-6	Different view of the sample in Figure 5-5 showing the looped structure that collects as the conical strand that extends to the right collapses.....	96
5-7	Fibers collecting on a single copper wire as a low density structure for 5 minutes.....	97
5-8	SEM images of nanofibers collected from solutions with vary conductivities.	97

5-9	Fiber diameter at varying concentrations of NaCl on a circular collector with diameter 8.5 cm and fibers collected on a single copper wire.	98
5-10	20% La doped SrTiO ₃ fibers	98
5-11	Electrospinning SrTiO ₃ :20% La nanofibers onto a rotating drum.....	99

LIST OF ABBREVIATIONS

ACAC	ACETYL ACETONE
BET	BRUNAUER-EMMETT-TELLER
CNT	CARBON NANOTUBE
DI	DEIONIZED
DMF	DIMETHYLFORMAMIDE
K_{APP}	APPARENT RATE CONSTANT
PVA	POLYVINYL ALCOHOL
PVP	POLYVINYL PYRROLIDONE
SEM	SCANNING ELECTRON MICROSCOPE
TEM	TRANSMISSION ELECTRON MICROSCOPE
XRD	X-RAY DIFFRACTION

Abstract of Dissertation Presented to the Graduate School
of the University of Florida in Partial Fulfillment of the
Requirements for the Degree of Doctor of Philosophy

ELECTRIC FIELD ENHANCEMENT OF PHOTOCATALYSIS

By

Michael John Laudenslager

May 2013

Chair: Wolfgang M. Sigmund
Major: Materials Science and Engineering

Photocatalysts are semiconductor materials that utilize light to improve the rate of chemical reactions. These materials are primarily used to degrade toxic compounds in aqueous systems. The most photocatalytically active of these materials are only able to absorb a small portion of the solar spectrum, limited to the UV range and have a low quantum efficiency. Therefore, finding methods that improve the photocatalytic activity of these materials is essential to applying them to practical systems. Previous research has shown that application of an electric field through supported photocatalytic systems increases the reaction rate via improving charge carrier separation. The internal electrodes in these systems are limited by the electrolysis of water at high voltages. To overcome this limitation, an alternate reaction setup was developed using an external electric field applied through air combined with a dispersed nanoparticle system. The trend of reaction rate change with applied electric field strength is discussed in terms of the Poole-Frenkel behavior, which is predicted from photovoltage studies, while other potential influences of the electric field are also discussed. This demonstrates that an improvement in reaction rate by as much as 120 % can be achieved in a P25 system. The ability of an electric field to influence a variety of photocatalytic systems that have

different charge transport properties is examined in several systems, including rutile, CNT/TiO₂, ZnO/TiO₂, and SrTiO₃ doped with 20 % La. This work describes the synthesis and characterization of the materials, as well as the change in performance with electric field strength. In addition, the development of photocatalytic nanofibers via the electrospinning process is discussed for use as supported photocatalytic systems. However, a significant departure from the standard electrospinning regime was encountered when heavily doped compounds are used leading to low density structures and complications to the electrospinning process. The key parameters controlling this behavior were found to be the solution conductivity and shape of the electric field. For a TiO₂ sol-gel system, the low-density electrospun meshes began to occur when the solution conductivity was increased with NaCl to 1270 $\mu\text{S}/\text{cm}$ and above. Methods to control and prevent this behavior are presented.

CHAPTER 1 INTRODUCTION AND BACKGROUND

Photocatalysis

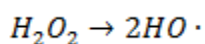
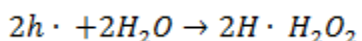
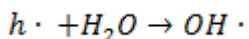
Water purification is a critical area of research in order to improve public health as well as maintain natural ecosystems. According to the World Health Organization, hazardous materials and bacteria in water systems are responsible for 4 % of deaths worldwide[1-2]. Lack of access to clean drinking water affects roughly 1 billion people[3]. These runoff pollutants not only affect human health, wildlife and aquatic systems also suffer deleterious effects[4]. Therefore, there is a significant need to further the development of methods to better understand and improve water purification methods.

The focus of this work is on the use of photocatalysis to remove harmful substances from water. Photocatalysts accelerate the breakdown of hazardous materials by harvesting light, which is used to generate free radicals. Photocatalytic materials are typically applied to three areas of water purification. The first area is removal of toxic chemicals from aqueous systems. Pollution remediation is especially important for the textile industry[5]. Between 1 and 15 % of the dyes used in textile manufacturing are lost in the process and can end up in effluents[6]. Photocatalysts are also commonly applied to bacteria removal and air purification[7]. Hoffmann et al. provide a more detailed discussion of the full range of environmental applications of photocatalysis[2].

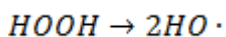
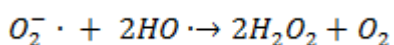
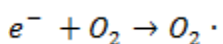
Photocatalysts absorb incident solar radiation with energy greater than their bandgap. The absorbed light excites electrons into the conduction band leaving holes behind in the valence band, depicted in Figure 1-1. These electron hole pairs can

become trapped or simply recombine; however, if separated, the photocatalyst can generate free radicals on its surfaces. The free radicals readily react with other compounds through redox reactions[8-10]. Both electrons and holes are capable of generating hydroxyl reactions with water as follows[11]:

Oxidative reaction:



The reductive reaction:



The photogenerated free radicals are then able to break down contaminants in the system.

Photocatalysts are typically semiconductor materials with bandgaps between 1-3 eV such as TiO₂, ZnO, WO₃, SrTiO₃, etc[12]. Figure 1-2 depicts the photocatalytic reaction of a P25 particle cluster with Procion Red on P25[13-15]. The reaction is initiated when the particle comes into contact with UV light. The light generates charge carriers inside the particle, which either recombine or transfer to adsorbed oxygen and water molecules. In both cases, hydroxide radicals are formed, as described in the previously mentioned oxidative and reductive reactions. The free radicals are then able to rapidly degrade other compounds, Procion Red, in this case.

There are several key limiting factors to photocatalysts. First, the bandgap energy of the most effective photocatalyst, TiO_2 , can only absorb in the UV region of light, which only makes up a small fraction of the solar spectrum. Second, the quantum efficiency of these materials are low due to a high rate of recombination[16]. Third, nanoparticles are the most highly active form of these photocatalysts, but are very difficult to recover. Therefore, new methods to improve the efficiency of these materials are needed for their practical application. The following sections provide a detailed background on photocatalytic properties with a focus on TiO_2 .

Surface Properties

High specific surface areas are needed for efficient photocatalysts because the reactions occur primarily on the surface. Charge carriers generated in the bulk generally recombine before they can contribute to the process. One of the primary influences on photocatalysis is the presence of surface oxygen vacancies. TiO_2 is typically oxygen deficient to varying degrees. Several studies show that oxygen vacancies trap electrons 0.75 eV below the conduction band[17]. However, only the vacancies that trap charge carriers near the surface, are effective at improving the photocatalytic ability of the material[18]. This helps further explain why smaller particles are more effective catalysts due to the higher surface area to bulk ratio. Furthermore, the oxygen vacancies allow adsorption of CO and O_2 molecules[19]. Adsorption of oxygen molecules is one of the essential steps in the photocatalysts process since it allows electrons to be removed from the material.

One of the challenges of forming reduced TiO_2 is that Ti^{3+} is not stable on the surface[20]. However, hydrogen reduction over several days creates a greatly disordered surface structure, which changes the color from white to blue to black over

time. Hydrogenation studies were initially conducted in 1964 to understand the transition from anatase to rutile, which is suppressed in vacuum and enhanced in hydrogen atmosphere [21]. A recent paper in Science found a practical application of this black TiO_2 as an efficient visible light photocatalyst that can also be used for water splitting[22]. The surface disorder, on the order of 1 nm induced by extended hydrogenation gives rise to mid bandgap states that are able to efficiently absorb a broad spectrum of light. Hydrogen atoms remain bonded with both Ti and O on the disordered surface, giving rise to its stability.

TiO₂: Anatase, Rutile, and the P25 Standard

TiO_2 exists in several phases; however, the most photocatalytically active are the anatase and rutile phases, shown in Figure 1-. Anatase has a higher bandgap (3.2 eV) than the rutile phase (3.0 eV). Despite the narrower bandgap of rutile, which provides a larger range of visible light adsorption, anatase is widely considered the more photocatalytically active material. Interestingly, mixtures of the two materials exhibiting the highest performance[23]. The enhancement effect is observed in both multiphase TiO_2 particles and through physically mixing anatase and rutile particles together. It has been shown that rutile is a highly active catalyst for some reactions, such as photolysis[24]. However, a combination of anatase and rutile is apparently critically important when oxygen acts as an electron acceptor[15].

There are several causes that give rise to this disparity in performance of the two phases. First, rutile is a phase that requires higher temperatures to form than anatase. This typically results in particle sizes that are substantially larger than anatase particles. The larger particle size greatly decreases the available surface area for the reaction to take place. Second, rutile exhibits a higher recombination rate[18, 25]. Third, anatase

has a higher adsorptive affinity for organic compounds than rutile[23]. Interestingly, Xiang et al. developed a low temperature synthesis allowing them to produce 5 nm diameter rutile particles, which reportedly exhibits over an order of magnitude superior performance compared to P25[26]; however, this might be due entirely due to the significantly higher surface area of rutile. Another consideration is that studies that report synthesizing “anatase” often actually have a small portion of rutile, and can take advantage of the synergistic effect between the two. Regardless, it is clear that there is a large synergistic effect when the two phases are present together.

The ability of mixtures of distinct anatase and rutile particles to improve photocatalysis has been further demonstrated by Su et al. They determined the optimum ratio of anatase to rutile is 60:40 by analyzing the photocatalytic performance of TiO₂ with identical grain size and surface area with differing ratios of the two phases[27]. Furthermore, heating P25 at 800°C to form an entirely rutile phase is associated with an order of magnitude loss in surface area, and a strong decrease in photocatalytic performance[28].

While numerous studies have demonstrated a significant improvement in the photocatalytic activity of combining anatase and rutile, the nature of the improved performance is debated in the literature with several conflicting models. Although, original theories suggested electrons traveled from the higher conduction band of anatase into rutile, newer theories suggest electrons travel in the opposite direction[23, 29] [16, 23]. The newer theories suggest that excitons generated in rutile are able to transfer electrons from the conduction band of rutile into trap states within the anatase phase, while holes remain within rutile trap states[23]. Oxygen trap states exist 0.75 eV

below the conduction band that acts as trapping sites for electrons and holes[17, 23]. Zhang et al. attribute the separation behavior to differences in work functions, 5.41 eV and 5.19 eV for anatase and rutile, respectively. The work functions lead to a higher Fermi level 0.22 eV in rutile than anatase[30]. The difference in Fermi levels generates an internal electric field that attracts electrons into the anatase phase. On the other hand, Sun et al. report there is an upward bending of the anatase conduction band preventing electrons from flowing from anatase to rutile, but still allowing holes to transfer to rutile[31].

P25, a mixture of anatase and rutile, is often used as a photocatalyst standard due to its high performance. The mixture is approximately 80% anatase, 20% rutile with a small amount of amorphous TiO_2 and a particle size of around 20 nm[15]. TEM studies show that anatase and rutile exist as distinct particles in agglomerates and not as multiphase particles[14] [15]. While many photocatalytic studies develop particles using a sol-gel process, P25 is developed through the Aerosil process. In this gas phase powder synthesis, titanium tetrachloride is hydrolyzed at elevated temperatures[13]. This process prevents the excessive aggregation and grain growth that are observed in many sol-gel synthesis routes, which allows the P25 particles to readily disperse in water. (1-2)

The electronic properties of the TiO_2 phases also gives hints to their differing performances. The electron mobility in various forms of TiO_2 is reported in Table 1-1[59] [60]. This table makes it clear that rutile has a substantially reduced electron mobility than the anatase phase. The prevailing theory for electron motion in TiO_2 comes from a polaron model[32]. In this model, conduction atoms become trapped in lattice

distortions. The trapped electrons are able to move between sites by a hopping mechanism that is strongly influenced by temperature[33]. The mobility for nanoporous particles is thought to largely be limited by transport between particles[34]. The average distance electrons and holes move in TiO_2 before recombining is known as its minority carrier length. Without the presence of an electric field, this value is 100 nm in TiO_2 [35]. Therefore, particles that are significantly larger than the minority carrier length will have a greater extent of internal recombination of charge carriers.

Simulations and experimental evidence have demonstrated that each crystal facet has a different reactivity. For example, in TiO_2 the {001} facet is more reactive, but surfaces are typically dominated by (101) surfaces[36-38]. The average surface energies for TiO_2 facets are {001}> {100}> {100} with energies of 0.90, 0.53, and 0.44 J/m^2 respectively[39]. These high-energy sheets are synthesized by using fluorine ions from hydrofluoric acid solutions to lower the surface energy of the {001} facets. Rutile generally does not predominately exhibit the high energy {001} face; rutile particles typically exhibit {011} and {110} faces[40]. The absence of the higher energy facet is likely a contributing factor to the lower reaction rate of rutile particles.

Methods to Improve Photocatalytic Performance

There are several often conflicting material requirements for optimizing photocatalysts. Further complicating photocatalyst research methodology is that, unlike solar cell research, there are no standard lighting or reaction conditions for photocatalysts. Typically, either UV or strictly visible light sources are used. However, many parameters that influence the activity change making it difficult to compare the results between seminal papers. However, Degussa P25 is typically used as a benchmark material with which to compare any novel compounds.

Several properties are critical for developing an efficient photocatalyst. Among these are: the ability to generate excitons over the desired wavelength range, the ability to efficiently separate electrons and holes, maintaining a high surface area for reactions to take place, and the ability to separate catalyst material from solution. While many photocatalysts are tested in the UV range (300-400 nm), this only makes up for 5 % of the solar spectrum. 43 % of the spectrum is in the visible range (400-700 nm), while the remaining 54 % is in the infrared range (700-2500 nm)[41].

Although TiO_2 is one of the most efficient photocatalysts, its band gap only permits absorbance ultraviolet range. Therefore, a large portion of the solar spectrum is not utilized by many photocatalysts. There is great interest in extending the range into the visible portion of the spectrum. There are several methods of doing so. Initial efforts focused on doping with cationic compounds. However, many of these dopants only served as recombination centers, reducing performance overall. On the other hand, recent progress on anionic dopants has shown significant improvements in performance.

Doping of various compounds has been extensively studied. Both metallic (Ca^{2+} , Sr^{2+} , Ba^{2+} , Al^{3+} , Ga^{3+} , Cr^{3+} , Fe^{3+} , Co^{3+} , Ce^{3+} , Ln^{3+} , Sn^{4+} , Zr^{4+} , Nb^{5+} , Mo^{5+} , Sb^{5+} , and Ta^{5+}) and nonmetallic ions (N^{3+} , C^{4+} , S^{4+} , F^- , Cl^- , and Br^-) have been investigated in a variety of configurations[41]. Self-doping of TiO_2 is also possible. The addition of an oxygen scavenging compound prior to heat treatment can result in Ti^{3+} sites in the bulk of the nanoparticles[20, 42].

One of the difficulties with evaluating these studies are that the method of doping can alter the performance[43]. This is due to dopants within the bulk primarily

acting as recombination centers. Ideally, the materials should be doped in such a way that the dopant exists predominantly in the surface[44]. Furthermore, whether the dopants exist as interstitials or substitutionals is influenced by the oxygen pressure during annealing[45]. Another complication with dopants is shifting of the bandgap. For example, dopants that shift the valence band upward may reduce oxidation efficiency, while increasing the reduction efficiency[44-45]. Therefore, materials with the same chemical constituents may behave very differently depending on the processing steps, the light spectrum, and the reactions catalyzed.

Photocatalyst Recovery

One of the greatest challenges to photocatalysts is recovery of the photocatalytic material. Nanoscale particles are required for high photocatalytic; however, removing nanoparticles requires long sedimentation times or very fine filters. Removal of particles from the system is impractical, and the nanoparticles themselves are potential health hazards[46]. Supported photocatalysts make the recovery process easier at the expense of significantly reducing the reaction rate. The inherently interconnected nature of supported photocatalysts has significantly lower surface area. Furthermore, diffusion of reactant species into the pores of the supported photocatalysts is significantly slower[47].

Another complication is that the support material itself typically interacts with the incident light, reducing the effect of the attached photocatalysts. It is possible to overcome some of the limitations of light penetration into photocatalysts by supporting the photocatalysts on fiber optic fibers to channel the light toward the catalytic material[48]. Other methods to improve the performance of supported photocatalysts include using carbon support materials, which enhances adsorption of pollutant

material, concentrating it around the photocatalytic TiO_2 , or applying an electric field[35, 49-50].

Electrospun fibers are often utilized as electrospun support materials. These fibers are typically on the nanoscale and can reach meters in length. The fibers entangle, forming a stable, but highly porous material. The non-woven meshes of nanofibers are often used as photocatalyst supports by incorporating nanomaterials into the fibers[51-52]. Alternatively, the photocatalytic material can be electrospun directly as a fibrous structure[53-54].

Alternatively, it is possible to utilize magnetism to recover specially developed magnetic photocatalyst particles. By coating magnetic nanomaterials in photocatalytic material, an applied magnetic field can fluidize and aide in recovery of the particles [55-57]. While magnetic coated particles allow recovery of highly dispersed photocatalytic systems, a new set of challenges is presented. The heterojunction between the photocatalytic surface and magnetic core often has a detrimental effect on photocatalytic performance[58]. A second challenge in developing magnetic photocatalysts is the core-shell structure greatly increases the particle size. However, magnetic photocatalysts remain a promising alternative to supported photocatalysts.

Photocatalytic Degradation of Dye Molecules

Dye molecules are commonly used as model degradation products in photocatalytic systems due to the practical application of removing them from effluent systems and the ease with which their degradation can be monitored. The nature of dye compounds requires high stability under a variety of conditions. The EPA reports the half-life of these dyes is around 2,000 h when exposed to sunlight[59]. There are several degradation products that result from dye color removal. Remaining products

include CO₂ and formic acid. However, these products are not considered hazardous and readily break down easily in the environment, unlike the dye molecules[6].

Photocatalytic activity is often extended into the visible range due to the photosensitization of the semiconductor by dye molecules used in the degradation reactions[60]. The singlet excited state of a dye molecule adsorbed on the surface of TiO₂ can transfer an electron into the conduction band of the TiO₂. The trapped electron is then transferred to adsorbed oxygen, creating O₂⁻ that generates reactive HO[•] and HOO[•] radicals[6, 61]. The experiments show oxygen is necessary to remove electrons for the process to proceed and is the rate limiting step. Without oxygen the dye simply regenerated. Galindo et. al suggest the photosensitization process might be responsible for 25% of dye degradation[6]. However, Muneer et al. suggest the photocatalyst is able to inject electrons into the dye, leading to its degradation[62]. The dye photosensitization mechanism also explains the ability of P25 to decolorize the dye material in visible light conditions. Photosensitization by dye molecules of the photocatalyst makes it essential to store the materials away from both visible and UV light prior to performing UV-vis analysis.

A third reaction can also take place on the surface of TiO₂ without any incident light sources. The surface chain radical mechanism where trapped electrons in the TiO₂ conduction band generate free radicals[63]. However, this effect is minor compared to the other two degradation mechanisms under normal circumstances.

Textile industries often release dyes into effluents. These industries require robust dyes that are resistant to biological and chemical degradation. When released into the environment, the dyes have a detrimental effect due to their toxicity and

mutagenic effects[64]. Therefore, dye degradation studies are useful in both practical applications and as a simple model for the effectiveness of photocatalytic materials.

Kinetic models based on surface adsorption are commonly used to analyze photocatalyst reactivity. Studies have suggested that TiO₂ surfaces preferentially adsorb certain functional groups[65]. Adsorption of the material that is being degraded is not a necessary condition for photocatalysis; however, different modes of adsorption affect the rate of degradation of different materials[66-67]. Although dye adsorption is not required, it does influence the degradation of dye material due to the proximity with the generated free radicals as well as through photosensitization as previously discussed.

The zeta potential and charge of the dyes as well as surface adsorption sites are critical for determining the ability of the dye material to adsorb on the photocatalyst surface[66]. The isoelectric point of P25 is around 6.2 with anatase and rutile reported to have similar values of 6 and 5.5, respectively[68-69]. However, a wide range of values is reported for both material phases. Studies show that different dyes have optimal absorption ranges at varying levels of pH on TiO₂ surfaces[70]. This suggests that both the photocatalyst and the surrounding conditions need to be optimized to achieve the highest degradation rates.

In order to determine the rate constants of photocatalysts, a variety of compounds are often degraded. One such material is Procion Red MX-5B, which is readily degraded by photocatalytic materials. The structure of the dye is shown in Figure 1-. The degradation rate is easily determined by following the changes in the dye intensity over time. The dye absorbs visible light up to 538 nm, which results in its distinctive color. The absorbance range is ideal for preventing screening of UV light by

the dye itself. However, this can become a factor in visible light photocatalysis. This particular dye is anionic, dissociating in water forming sulfonate groups. The sodium groups in Procion Red dissociate leaving behind a negatively charged compound. The negative charge of the dye influences its ability to adsorb onto the catalyst surface. Several factors influence the dye degradation rate of Procion Red, including pH and initial dye concentration[71].

The dye degradation of Procion Red has been extensively studied and is outlined here. OH radicals initiate the process by cleaving the carbon-nitrogen double bond[72]. The organic dye compounds formed are mainly CO₂ gas and benzene. Other compounds formed include Cl⁻ and SO₄²⁻. The degradation of the organic compounds was found to correspond very closely to the color removal in the system for Procion Red[73]. The degradation of various dye molecules all follow similar kinetic models as described in the following section.

Reaction Kinetics

The reaction rate of dye degradation studies are typically described by using the Langmuir Hinshelwood model of surface kinetics as outlined below[74-76]. This treatment of the degradation does not take into account the individual steps in the reaction such as the rate of adsorption or individual reaction steps. Only the overall reaction rate, k_{app} is considered. However, due to different experimental conditions such as quantity of materials, type of dye, light source, etc. it is difficult to compare reactions from different studies. A description of the mathematical derivation of the Langmuir Hinshelwood kinetics follows starting from the standard rate is equal to change in concentration divided by time ($r = dC/dt$).

r=reaction rate

C=dye concentration

K=rate constant

K=adsorption constant

K_{app} =apparent rate constant

Assumptions:

Dye concentration goes to zero $C \rightarrow 0$

$$r = dC/dt = kKC/(1+KC)$$

$$1/(KC_0) \ln(C/C_0) + (C/C_0 - 1) = -kt/C_0$$

Assuming $C \rightarrow 0$

$$1/(KC_0) \ln(C/C_0) \gg (C/C_0 - 1)$$

Therefore:

$$\ln(C/C_0) = -Kkt$$

$$C(t) = C_0 e^{-k_{app}t}$$

$$C(t) = C_0 e^{-t}$$

Parameters That Influence Photocatalytic Reaction Rates

In order for comparisons between photocatalytic studies to be valid, the reaction conditions must be held constant between experiments. Photocatalytic reactions appear to be relatively insensitive to changes in reaction temperature[77]. However, typically, reaction rate decreases with increases in temperature[78]. The decreased reaction rate

is due to increased desorption of adsorbed reactant species and higher rates of recombination.

The solution pH alters the surface charge, which will influence adsorption on the photocatalyst. In addition, the pH can also lead to the dissociation of the adsorbing molecule as well as other effects. Therefore, pH will affect varying compounds differently, and no single general trend is observed[79].

Anions and cations alter the zeta potential of TiO_2 . Altering the point of zero charge has the potential to enhance the photocatalytic reaction by improving the affinity of the reactant species with the catalyst. However, studies from a wide variety of cations and anions including NO_3^- , Cl^- , HCO_3^- , CO_3^{2-} , SO_4^{2-} , HSO_4^- , H_2PO_4^- , decrease overall performance[80]. The salts reduce the available surface area for dye adsorption slowing the reaction rate overall.

An important consideration in the reaction rates of photocatalysis materials is the method in which various materials are compared. Photocatalytic studies tend to report reaction rates using equal masses of all compounds. It is also possible to report the reactivity based on a surface area basis. This partially accounts for differences in particle sizes between different samples and gives a better idea of the photocatalytic activity per area of exposed surface. For example, doping materials often hinder particle growth, resulting in a much greater surface area than pure TiO_2 . In many of these studies, it is likely any enhancement in the photocatalytic activity was merely due to synthesizing smaller particles.

Particle Size and Morphology Analysis

One of the largest influencing factors of photocatalytic activity is the surface area of photocatalytic particles. Chemical modifications to photocatalyst materials often

change both their particle size as well as surface properties. Comparison of materials based on surface area is necessary in order to determine if photocatalytic activity changes are due to changes in chemistry or due to an increase in overall surface area. Scanning electron microscopy and transmission electron microscopy are typically used to determine particle morphology. While the grain size and surface area are determined from X-ray diffraction and BET surface area measurements.

The fraction of anatase to rutile is determined through XRD analysis. The weight fraction (W_R) corresponds to Equation 1-1 **Error! Reference source not found.**, where A_A and A_R are the intensities of (101) anatase and (110) rutile peaks[81]:

$$W_R = \frac{A_R}{0.884A_A + A_R} \quad (1-1)$$

Similarly, the average particle size is determined from line broadening effects based on the Scherrer equation, Equation 1-2, where L is the crystallite size, λ the X-ray radiation wavelength (0.15418 nm), β is the line width at half maximum, and θ the diffraction angle of the diffraction peak[82]:

$$L = \frac{0.89\lambda}{\beta \cos(\theta)} \quad (1-2)$$

Zeta Potential

Stability and dye adsorption in photocatalytic systems is affected by the surface charge of the particles. The surface charge of photocatalytic systems is dependent on the pH of the solution. Charged particles repel each other, which helps maintain their dispersion. Depending on the pH, the surface charge can be positive, negative or zero depending on the material system. The point of zero charge for TiO_2 is reported in the pH range of 3.5-6.5, depending on the combinations of phases present[83].

The degradation material that is studied will also have an electrostatic interaction with the photocatalytic material. Dyes may be either positively or negatively charged in solution. However, in general, proposed mechanisms of photocatalysis do not require dye molecules to directly interact directly with the TiO_2 surface except in the case of photosensitization. Lee et al. report that altering the pH of photocatalytic systems decreases overall rate constants. Higher and lower pH values decreased the overall reaction rate to around half this value[84]. Their analysis states that electrostatic repulsion is not the main reason for the lowered reaction rate, but instead a lower production of hydroxide radicals in the acidic/basic conditions.

Electric Field Effects on Photocatalysts

Several different phenomena generate electric fields that influence photocatalysis. Electric fields can be “internal” where they occur due to contact between photocatalysts materials and surrounding chemical molecules. Alternatively, a power supply can be used to generate an “external” electric field. Both types of electric fields are commonly used to influence charge transport within the photocatalytic materials as discussed in the following sections. The presence of electric fields in photocatalytic systems help separate charge carriers and to mobilize trapped electrons [85-86]. The improvement in charge transport improves the overall reaction rate of the photocatalytic materials.

Internal electric fields

Internal interfaces between different phase regions and in composite materials leads to the development of an electric field. The high activity of P25 is, in part, due to the mixed anatase and rutile phases of TiO_2 . Similarly, CNT/ TiO_2 structures form a Schottky barrier at the semiconductor metal junction, which helps enhance exciton

separation[87]. In supported TiO₂ systems, Lana-Villarreal et al. observed a long range electric field throughout the TiO₂ layer[88]. An electric field also forms due to the charge transfer between adsorbed polar water molecules and the photocatalyst. This electric field transports electrons into the bulk, while holes move to the surface[89].

External electric fields

External electric fields are produced from an external power supply. These electric fields can produce a significant enhancement in photocatalytic performance[85-86]. Photocatalytic systems are complex and electric fields can have potential effects on several parameters. Therefore, it is important to take each into consideration before applying theories to understand the behavior. An applied electric field can accelerate the photocatalyst particles, cause water to split into hydrogen and oxygen, alter dye adsorption, alter electron mobility, and enhance electron-hole separation[85, 90-91].

Figure 1- demonstrates the acceleration and orientation effects of an electric field on a P25 nanoparticle cluster. Electrophoresis is the study of the effects of electric fields on the motion of particles. The following section discusses the key parameters to the motion of particles in an electric field, including the particle mobility, and acceleration. The electrophoretic mobility of particles (μ_s) in an electric field is described by the Smoluchowski equation, Equation (1-3), where ϵ_0 is the permittivity of free space, ϵ_r is the relative permittivity of the surrounding media, ζ is the zeta potential, and η is the viscosity of the surrounding media[92].

$$\mu_s = \frac{\epsilon_0 \epsilon_r \zeta}{\eta} \quad (1-3)$$

Charged colloids in electric fields accelerate, which can influence their dispersion, and therefore catalytic performance. Conversely, it could also lead to

aggregation, and decrease performance depending on the electric field strengths and materials involved. This acceleration can improve particle dispersion or simply cause particle deposition on the electrode. The time for the particles to reach a constant velocity is described by Equation (1-4), where ρ , and η are the density and viscosity of the liquid, and a is the particle size[93] :

$$\tau = \frac{\rho a^2}{2\eta} \quad (1-4)$$

For nano-sized particles dispersed in water, this equation yields a maximum velocity within a nanosecond timeframe.

The aforementioned equation assumes the particles are uniform. Often, photocatalytic particles are aggregates of mixed phases or composite structures. Furthermore, the particles typically exist as clusters even when dispersed in liquid. This results in a nonuniform zeta potential, which creates both a translation and rotational component to the effect of the electric field[94]. In general, the interactions with nonuniform particles are complex and subject to a number of modeling and experimental studies[92, 95]. The interactions of anisotropic particles in an electric field include alignment or pairing of particles, rotational, and translation motions.

Typical photocatalytic systems undergo stirring for two purposes. Stirring the photocatalytic reaction prevents diffusion from limiting the reaction rate. It also has the added effect of maintain particle dispersion in systems that do not disperse well. A study conducted on the competing effects of viscous forces and electric fields on nanoparticle motion suggests that the effect of a stir bar will overcome any acceleration effects of the electric fields even at very low stirring rates[96]. Alternatively, particle acceleration cannot occur at all in supported photocatalytic systems. This suggests that particle

acceleration alone will not have a significant impact on changes in photocatalytic activity.

Electrolysis, the splitting of water to hydrogen and oxygen, can also occur if a high current is applied to the system[97]. The reaction typically requires high current density as well as an electrolyte to increase the conductivity of water. Photocatalytic studies involving electric fields do not use electrolytes and typically use very low current densities, which prevents the competing electrolysis reaction[98]. If electrolysis were to occur, it would remove water from the system, which increases the dye concentration. A decrease in water content increases dye concentration. The increase in concentration would appear to make the photocatalysts less active.

Besides physically accelerating colloidal particles, an externally applied electric field alters the electron mobility within the particle. Note that this is a distinct property from the previously mentioned mobility of the particle itself. Electrons in TiO₂ move via hopping between localized states[99]. The movement is dependent on temperature and applied electric field strength. With higher electric fields being able to release electrons trapped in Coulomb potential wells[100-101]. In polycrystalline materials, this effect follows Poole-Frenkel behavior, described in Equation 1-5, where μ and F are the electron mobility, applied electric field, and Y is a temperature dependent constant[102-104]:

$$\mu(F) = \mu_0 e^{Y\sqrt{F}} \quad (1-5)$$

$$\sigma = e(n\mu_e + p\mu_h) \quad (1-6)$$

Furthermore, conductivity is related to the mobility through Equation 1-6, where e , n , p , μ_e , and μ_h are the elementary static charge, the number density of electrons and holes, and the mobility of electrons and holes, respectively[105]. Therefore $\sigma \propto e^2 n \mu_e + p \mu_h$.

Poole-Frenkel behavior has been used to describe the photogeneration of charge carriers in rutile. Itoh et al. demonstrate that electric fields increasingly enhance photoconductivity of rutile in the range of 50-250 V/cm[85]. A slight increase was observed below 50 V/cm, and a gradual decrease was observed above 250 V/cm. The authors suggest the increase in photoconductivity suggests that it should enhance photocatalytic performance in a similar fashion. Poole-Frenkel behavior typically presents a linear range at low electric field strengths and a non-linear region at high electric fields[106].

Other mechanisms for enhanced charge transport also exist for semiconductor materials. The Schottky and Ohmic mechanisms have also been reported for nanomaterial devices in electric fields depending on the field strength[107]. It is generally reported the Schottky currents and Ohmic conduction occur primarily in low field strengths[108]. The distinction between the different behaviors is typically determined based on which of the three models it fits.

Electric field effects on exciton separation

The presence of an external electric field does not influence photon adsorption or the initial generation of excitons; instead, the external field influences their separation[109]. There is a threshold electric field strength below which the electric field will not significantly influence separation of electron hole pairs[110]. Several studies have shown preliminary work on the effects of electric fields on TiO₂. Itoh et al.

demonstrate that an electric field enhances the photoconductivity of rutile at 4K[85].

Jiang et al. created a thin film photocatalytic material and studied the effects of electric fields. In their study, electrodes were placed inside the container, and low voltages were run through the system. They report that the effect levels off at very low field strengths, on the order of 1-2 V/cm[86], and suggest photolysis becomes a competing reaction at higher voltages.

Electric fields can also influence surface adsorption. During the process of photocatalysis, the rate determining step is the electron transfer from the semiconductor material to the oxygen in solution. The electron transfer step also has the side effect of rendering the photocatalyst negatively charged[111]. Application of an electric field removes electrons from the system, reducing recombination, and creating a positive surface charge, which attracts reacting molecules[111]. Procion Red, the dye used in the following experiments also dissociates in water to form a negatively charged compound. However, adsorption of the dye material onto the surface is generally not reported as a necessary step in photocatalytic reactions.

Another reported effect of external electric fields is that they can improve charge transfer in composite materials where the activation barrier is normally too high for the phenomenon to occur[112]. White et al. demonstrated that a ZnO/TiO₂ composite material could be induced to transfer charges from TiO₂ to ZnO in photovoltaic materials only when the electric field strength was high enough. At lower field strengths, the composite system only served to enhance recombination. The effect makes certain materials interesting in the presence of an external field that would make poor photocatalysts under normal circumstances.

Sol-Gel Processing of Nanomaterials

The sol-gel process is one of the most common methods to synthesize novel photocatalysts. This process is useful for photocatalysis synthesis due to the high purity of the precursor materials and the ability to control many of the synthesis parameters such as particle size. A typical sol-gel process for a TiO_2 precursor is shown in Figure 1-. In the first step, the metal alkoxide reacts with water to form hydroxyl radicals. The hydrolyzed materials are then able to react with each other in a condensation step. This second step forms the necessary metal-oxygen bonds and liberates water molecules. The network that forms is dependent on several factors such as the solution pH and the ratio of water to metal alkoxide it is exposed to[113].

One of the major drawbacks of alkoxide solutions is their stability. Even small amounts of moisture will cause the reaction to proceed. Equation 1-7 shows the parameters that are responsible for gelation time:

$$tg = [C_o k(f^2 - 2f)]^{-1} \quad (1-7)$$

Where tg is the gelation time, c_o is the initial concentration, k is the condensation rate constant and f is the apparent functionality of the alkoxide[114]. This equation is only valid when the rate of hydrolysis is significantly faster than the rate of condensation. The rate of hydrolysis is highly dependent on the length of the alkyl chain, where the rate is faster for shorter chains, i.e. ethoxide >propoxide>butoxide.

Chemical additives have many effects on the stability of alkoxide solutions. Gelation can be hindered in titanium alkoxides by using amines[114]. Acetic acid is commonly added to titanium alkoxide precursor solutions used for electrospinning. In this process, acetic acid prevents precipitation, although acids typically act as catalysts in sol-gel processing[115]. In the case of acetic acid with TiO_2 , an exothermic reaction

occurs where the acetate groups bond to the titanium acting as chelating and bridging ligands. Kessler et al. provided an in depth discussion on the interactions stabilizing agents have on sol-gel systems. The addition of stabilizing compounds produces an exothermic reaction, which is largest for acetylacetone, then triethanolamine, then acetic acid. Similarly, the stability of these compounds is that acetylacetone is most stable followed by triethanolamine and acetic acid.

The compounds stabilize the sol-gel process by increasing the charge distribution, which is evident by increasing the metal-oxygen bond lengths. The chelating ligands do not form a stable bond with the compound. Instead, they rapidly transfer between metal atoms, a process that is accelerated when alcohol is used as a solvent. Counterintuitively, these compounds actually increase the rate of hydrolysis and polycondensation. The process actually limits gelation by altering the pathway to polycondensation [116] [114].

Electrospinning of Nanofibers

Electrospinning forms non-woven fibrous meshes of polymer and ceramic materials. This process has three very distinctive features. First, electrospinning produces materials at a significantly smaller scale than other fiber production techniques. The fibers can be as small as tens of nanometers. Despite the narrow diameters, electrospun fibers can reach lengths of meters. Second, the technique is not limited to a specific array of materials. A large range of soluble polymers, sol-gel materials, and dispersed nanoparticle system can be electrospun into nanofibers[117-122]. Additionally, modifications to the electrospinning apparatus and the ambient conditions allow many modifications to the resulting material morphology and orientation.

A typical electrospinning apparatus is shown in Figure 1-8. To form fibers, the syringe is loaded with a viscous polymer solution. An advancement pump extrudes a liquid droplet at the tip of the needle. An electric field deforms the droplet into an elongated shape known as a Taylor cone. At a certain field strength, the droplet will begin emitting material that is accelerated toward a grounded collection plate. The ejected material can either be droplets or continuous fibers depending on chain entanglements in the polymer system[123-125]. The thin fibers allow rapid evaporation of the solvent as they whip around toward the collection plate.

An outline of the publication records is shown in Figure 1-. The study of this field begins around 1600 when William Gilbert first observed that droplets deform when applying an electric field[126]. In 1882, Lord Rayleigh published a theoretical model that predicts the electrical field strength needed to make a droplet eject fluid[127]. Sir Geoffrey Taylor began a new wave of publications in the field with his examination of electrostatic droplet deformation. In homage to his work, the distinctive droplet shape became known as a Taylor cone[128]. After researchers developed an understanding of this field, industrial developments making use of the technology began[129]. Two patents were published in 1902, which discuss methods to electrically disperse liquid droplets[130-131]. The concept of electrospinning was later patented in 1934[132]. Petryanov-Sokolov first realized the potential of electrospun fibers in filtration and created the first known industrial venture utilizing electrospun nanofibers. The entire field of electrospinning began to undergo rapid developments in 1990, which is also when the term “electrospinning” was first used to describe the phenomenon. Starting in 2002, another breakthrough in electrospinning occurred: the development of

electrospun ceramic nanofibers[133]. This progress opened the field to a range of new applications with particular interest in the energy harvesting and storage fields[134].

Models of the Electrospinning Process

The diameter of electrospun fibers is of critical importance to most of their applications. However, numerous parameters exist which influence the fiber diameters. Several theoretical models exist which predict the diameter of electrospun fibers. The final fiber diameter is governed by several parameters described by Equation 1-8. The solution properties, viscosity(η) and surface tension (γ), gravity, and the electric field strength govern the shape of the Taylor cone. The whipping motion the fibers undergo also affects the fiber diameter dependent on the radius of curvature in relationship to the diameter of the jet (χ). Other parameters include the dielectric constant of the outside medium (ϵ), the current (I), and the flow rate (Q). Fridrikh et al. developed an analytical model that accurately predicts fiber radius (r_{terminal}) for polymer systems[135] shown in

$$r_{\text{terminal}} = \left(\gamma \epsilon \frac{Q^2}{I^2} \frac{2}{\pi(2 \ln \chi - 3)} \right)^{\frac{1}{3}} \quad (1-8)$$

Ceramic Nanofibers

Ceramic nanomaterials are particularly interesting to photocatalytic and electronic device fabrication. Recent publications have explored solar cells, battery materials, thermoelectrics, and supercapacitors[134]. Ceramic fibers are prepared by adding precursor materials to polymer systems. The polymer allows the necessary chain requirements to form fibers to be met, which forms composite materials. Sol-gel systems and nanomaterials are often incorporated into these systems[136]. Calcination

of the resulting fibers burns out the polymer allowing the formation of purely ceramic nanofibers.

Ceramic precursors and composite systems have higher conductivity than typical polymer systems. The higher conductivity alters several of the underlying assumptions in the previously mentioned equation; however, a model exists that accommodates for these changes[121]. One important consideration that exists in ceramic systems is that the ratio of precursor material to the carrier polymer strongly influences the final fiber diameter. After calcination, the fiber diameters typically decrease to half of what they were in the green state. Figure 1-10 shows a typical electrospun fiber system for TiO_2 nanofibers. As the fibers are calcined, relatively smooth fibers are initially formed. At higher calcination temperatures, grain growth leads to fiber granularization.

Salt Loaded Polymers

Although sol-gel solutions are typically based on metal alkoxides, many precursors contain salt loaded polymers, which can be used to develop ceramic systems. In a typical process, salts are slowly added into a polymer solution. The dissolved salts are expected to greatly increase the conductivity of the electrospinning solutions. Highly conducting electrospun fibers behave differently from fibers with lower conductivity[121]. For highly conducting compounds, fibers often do not collect properly on the substrate. These effects are discussed in later sections. Salt loaded electrospun fibers have been produced of the following materials: NiTiO_3 , $\text{Al}_4\text{B}_2\text{O}_9$, $\text{Al}_{18}\text{B}_4\text{O}_{33}$, CeO_2 , Mn_2O_3 and Mn_3O_4 , and Co_3O_4 [121, 133, 137-140].

Electrospun Fiber Modifications

Although the fibers presented above have typically uniform, circular crosssections, a variety of electrospinning parameters will lead to significant departures in the morphology. A wide range of alternative electrospinning setups have been developed to attain different fiber morphologies. These methods typically employ modified collection electrodes. However, other methods have manipulated the electric and magnetic fields to alter the fiber morphology. Another major advancement comes from co-electrospinning techniques, which have been used to produce hollow structures as well as core-shell, and hollow-core-shell structures[141-142] [143-144]. Although fibers are typically not oriented, methods to align the fibers also exist[145-165]. Alignment techniques function by manipulating the shape of the electric field or simply collecting the fibers on a high speed rotating drum[149, 157-158, 160, 166]. The modifications to electrospinning setups lead to a diverse range of electrospun structures. However, altering the chemistry of electrospun solutions can also give rise to different fiber structures.

Electrospun fibers do not always produce uniform diameters. In some material systems, beads form periodically throughout the fiber. Low viscosity, low electric fields, and high surface tension fluids encourage bead formation[167]. Although beaded fibers are generally not desirable, Acatay et al. have shown beads improve the performance of certain hydrophobic materials[168].

Another related topological feature in electrospinning is the formation of branched structures. Unlike beading, which can be a difficult phenomenon to avoid, branched fibers only arise under very special conditions. In these structures, relatively short, thin structures appear along the sides of the fibers. These branches are due to

perturbations in the cross sectional areas of the fibers produced from highly viscous solutions in strong electric fields[169].

While typical nanofibers have circular cross sections, it is possible to electrospin fibers that are flattened. This change from a one dimensional to two dimensional material creates a number of interesting opportunities for study. In most reported studies, nanoribbons are produced by tailoring the solution properties as opposed to modifying the electrospinning apparatus. However, Yu et al. produced TiO_2 nanoribbons by modifying the spinneret tip shape[170]. One proposed mechanism for TiO_2 ribbons is that under very specific conditions a skin forms on the outer surface of the material as it is electrospun. This skin then collapses leaving behind flattened structures.

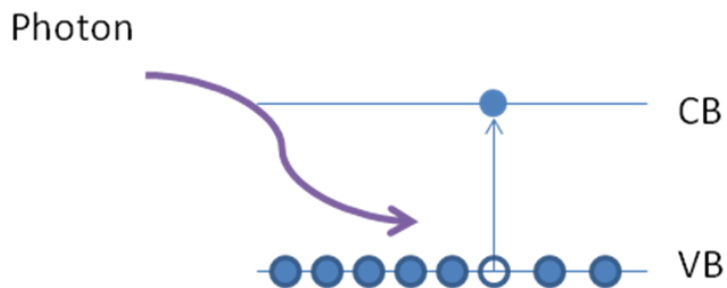


Figure 1-1. Band structure of a photocatalyst showing exciton generation in response to UV light.

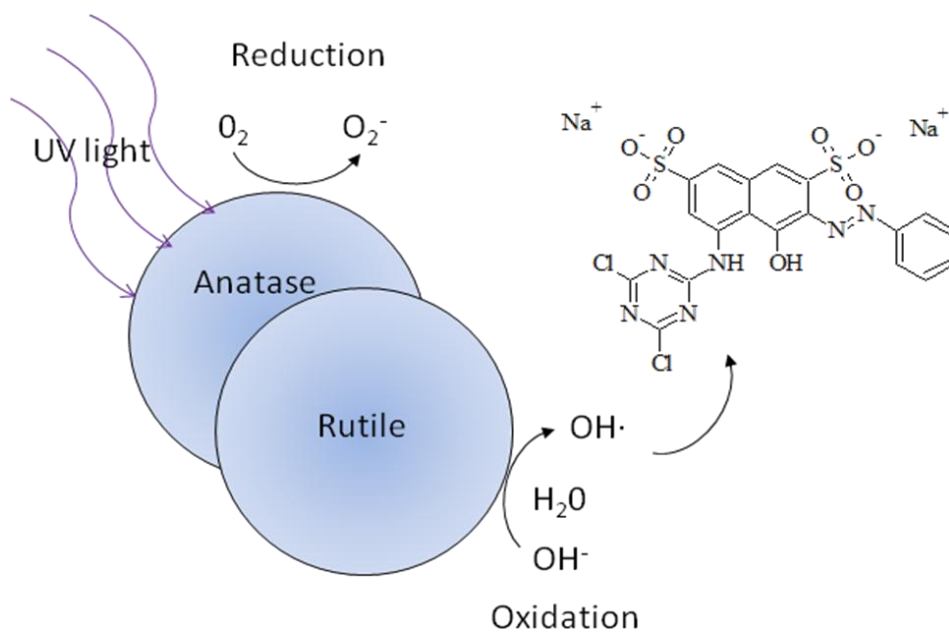
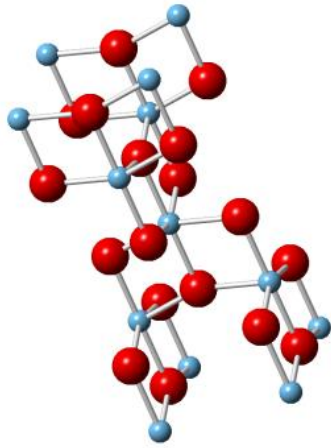
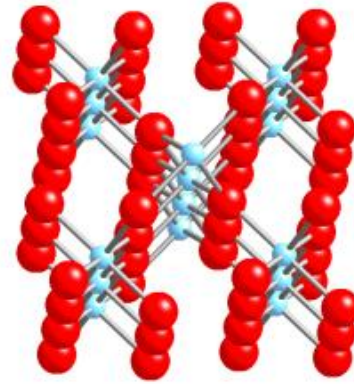


Figure 1-2. Photocatalysis of Procion Red dye on mixed phase TiO₂ particles.



A)



B)

Figure 1-3. Crystal structures of TiO_2 showing the two most common phases. The diagrams depict (A) anatase and (B) rutile. Ti atoms are red, while O atoms are blue.

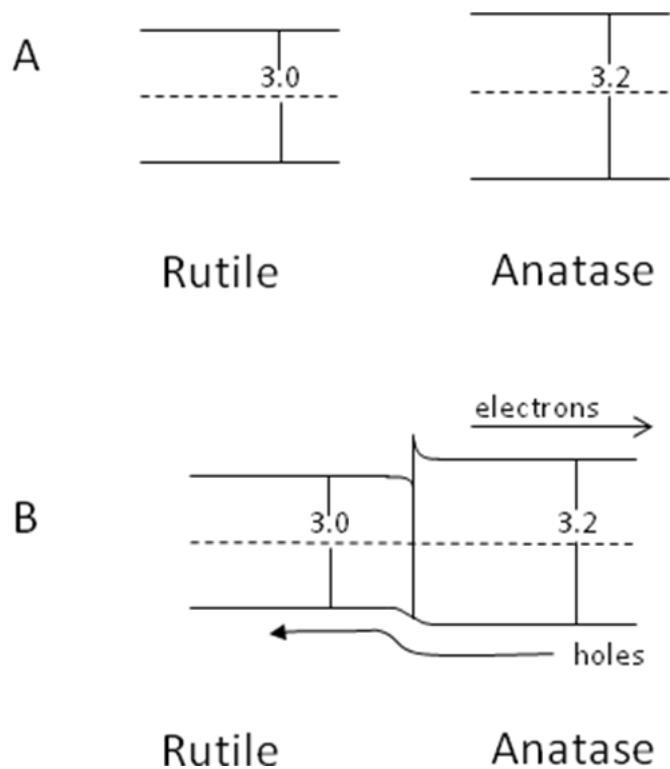


Figure 1-4. Band structures of anatase and rutile phases. A) Band structure of separate anatase and rutile particles. B) Upward bending of anatase conduction band when the two phases are in contact showing the direction of electron and hole movement.

Table 1-1. Electron mobility in various forms of TiO₂ materials.

TiO ₂ Structure	Electron mobility (cm ² V ⁻¹ s ⁻¹)
Anatase (single crystal)	100
Rutile (single crystal)	1
Porous TiO ₂	10 ⁻²
Nanoparticle TiO ₂	7X10 ⁻⁶

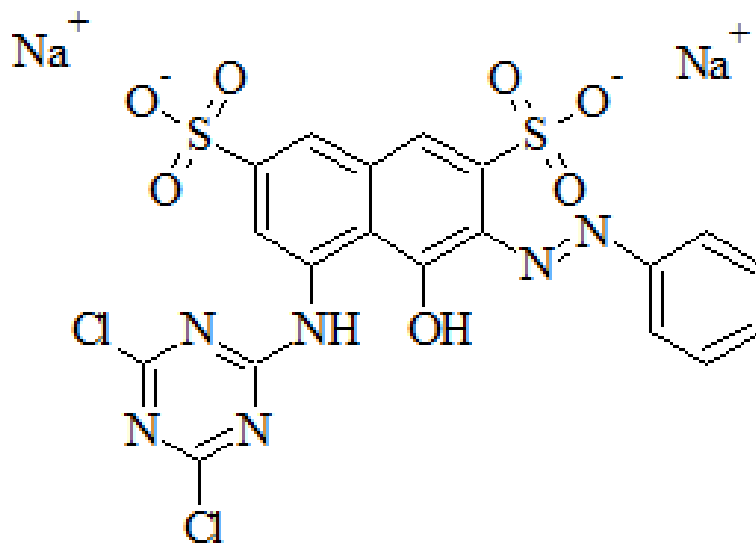


Figure 1-5. Procion Red MX-5B dye molecule.

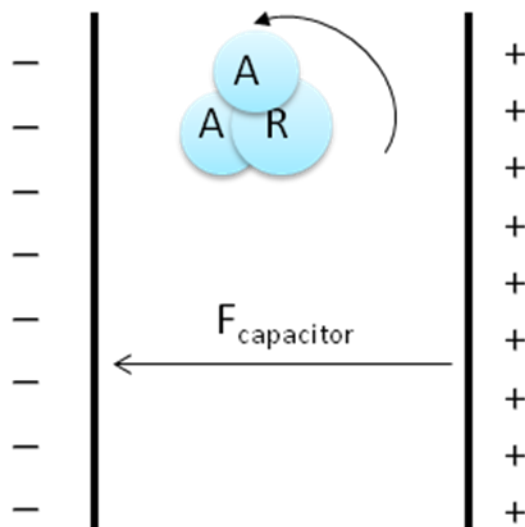


Figure 1-6. Nanoparticle cluster being oriented and accelerated by an electric field.

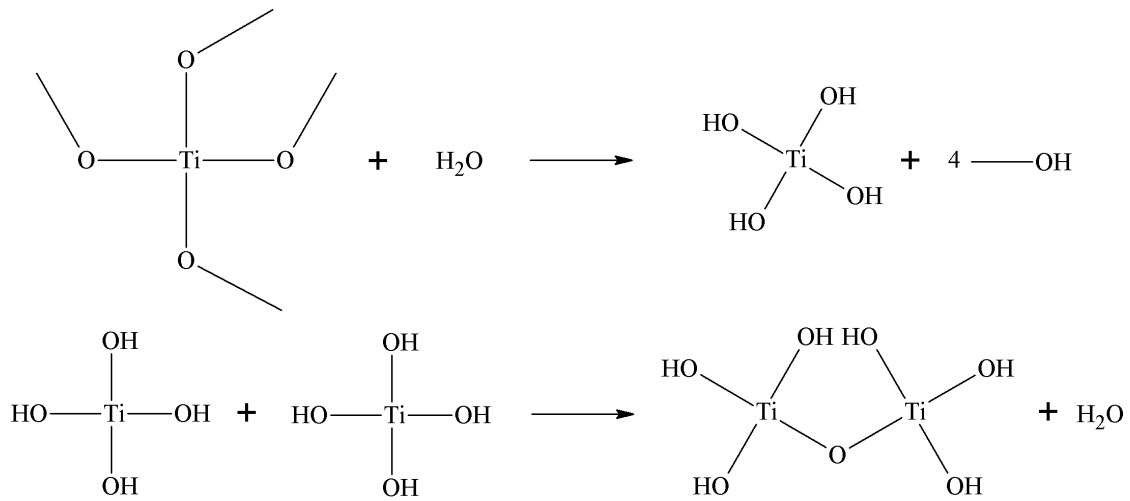


Figure 1-7. Hydrolysis and subsequent condensation reaction of titanium methoxide.

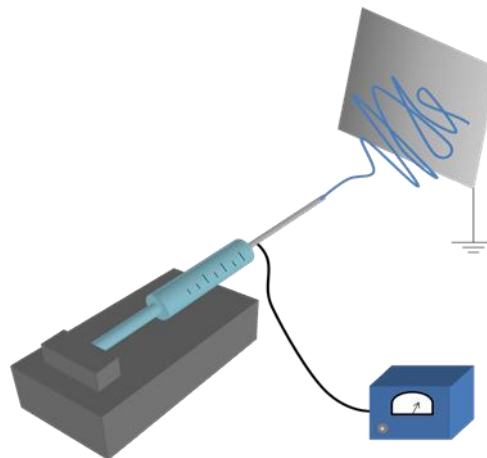


Figure 1-8. Diagram of a typical electrospinning apparatus.

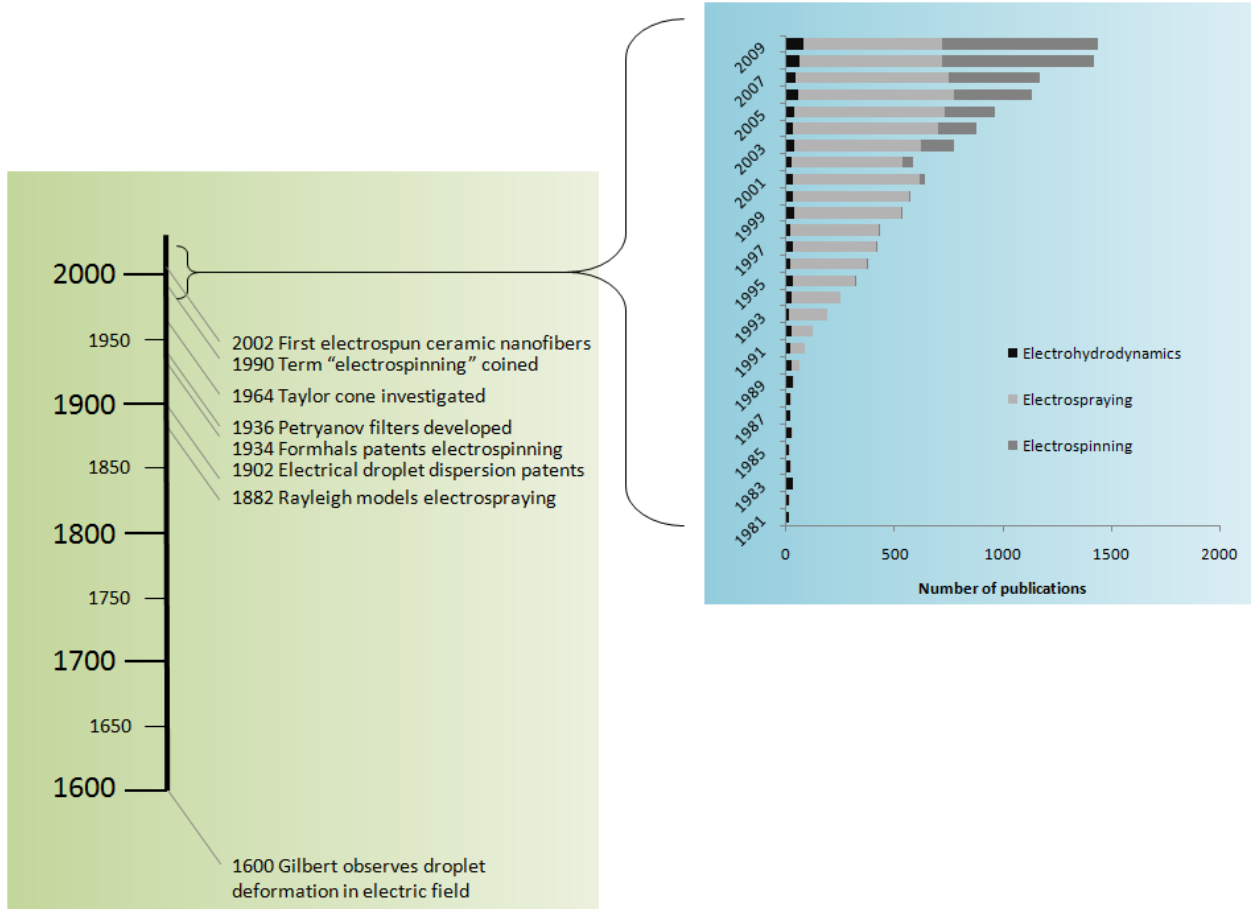


Figure 1-9. Timeline of the publication record on electrospun materials.

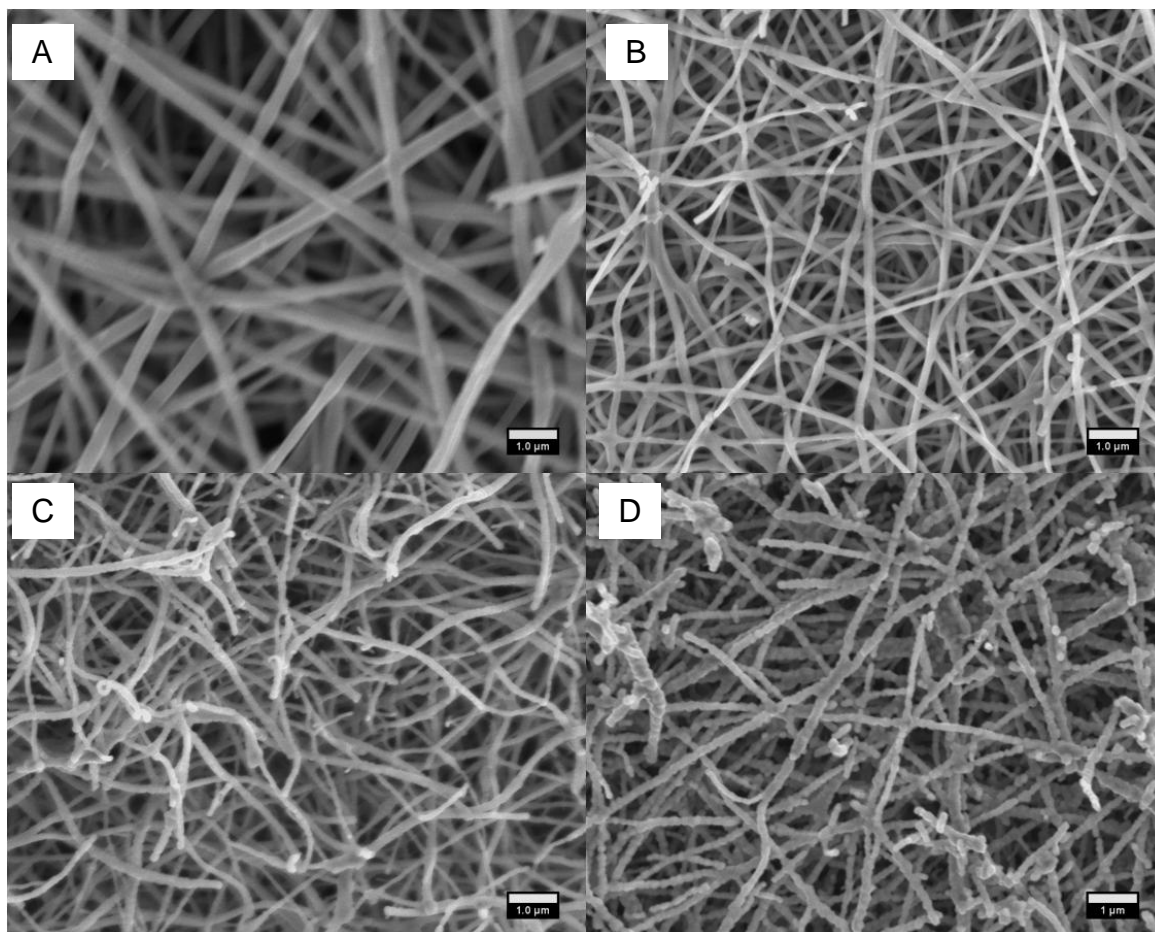


Figure 1-10. SEM images of as-spun electrospun TiO_2 nanofibers at various stages during the annealing process. (A) As-spun fibers, (B) fibers annealed for 2 hours at temperatures of 500°C , (C) 800°C , and (D) 1000°C . All images are at the same scale.

CHAPTER 2 MATERIALS SYNTHESIS AND CHARACTERIZATION

Synthesis of Photocatalytic Materials

Several material systems were tested to better understand the influence of electric fields on photocatalytic systems. Each material was selected for a specific reason as discussed in subsequent sections. The synthesis methods of the materials are discussed as follows.

P25. Degussa Aeroxide P25 is a commercially available material that is the standard of comparison in photocatalytic measurements. The P25 particles were used as-received without further modifications except where noted.

Rutile. Rutile particles were formed by heating P25 particles to 800°C for 3 h. This method was chosen to keep the properties of rutile as close to P25 as possible.

CNT/TiO₂. CNT/TiO₂ particles were prepared as follows. Titanium isopropoxide (98+%) and ethyl alcohol (200 proof 98+%) were purchased from Acros. Nitric acid (70% v/v) was obtained from Ricca Chemical Company. OH-functionalized multiwalled carbon nanotubes were obtained from Nanostructured & Amorphous Materials, Inc. (>95% purity). The MWCNTs have an outer diameter of 8 nm and a length of 0.2-2 μm. The following synthesis procedure was used to form the composite materials. Ethanol (50 mL) was added to DI water (0.5mL) and adjusted to 2 pH with nitric acid (0.5 mL 70 wt %). MWCNTs (0.4g) were then added to the mixture. A Mixonix Sonicator 3000 sonicated the samples for 10 minutes at a power level of 72 Watts. While stirring, titanium isopropoxide (7.1 g) was slowly added to the solution. After stirring for 12 hours, the solution was dried at 80°C and crushed prior to heating to 500°C for 4 hours.

ZnO/TiO₂. Particles were synthesized in a similar manner to the work of Liao et al[171] with a Ti:Zn mole ratio of 1:0.25 prior to heating to 600°C for 3 hours.

SrTiO₃: 20% La nanorods. Electrospun nanorods were electrospun as follows: PVP was dissolved in DMF (12 mL). AcAc (0.5 mL) was added followed by titanium isopropoxide (0.53 g). In a separate container, strontium nitrate (0.6 g) and lanthanum (III) nitrate hexahydrate (0.6 g) were dissolved in deionized water (2 mL). The two containers were then mixed prior to electrospinning with a field strength of 2 kV/cm. Samples were then heat treated in a flowing argon (0.5 mm Hg) atmosphere at 1100 °C for 12 hours.

Material Characterization

The photocatalytic materials were characterized to confirm the results of the synthesis techniques and to better describe the properties that influence the photocatalytic rates of the materials. Crystal structure and phase information was obtained through X-ray diffraction using a Philips APD 3720 diffractometer. Image analysis was performed on SEM images from a JEOL 6335 field emission SEM and a JEOL 200CX TEM. ImageJ software was used for image analysis. Surface area was determined through BET measurements using a Quantachrome NOVA 1200. Dye absorption spectra were measured via a Perkin-Elmer Lambda 800 spectrometer, while solution conductivity was measured with an Accumet Research AR50 Dual Channel pH/ion/conductivity meter. A detailed discussion of the results of the characterization methods follows.

X-ray diffraction of the P25 and rutile compounds reveals the expected mixed anatase and rutile phases for P25, and a purely rutile phase for the heat-treated material, shown in Figure 2-1. The ratio of anatase to rutile is determined through XRD

peak analysis described in Equation 2-1. This equation reveals the ratio of anatase to rutile, where I_A and I_R are the strongest XRD peak intensities of anatase and rutile, respectively[172]:

$$Anatase (\%) = \frac{100}{1 + 1.265 \frac{I_R}{I_A}} \quad (2-1)$$

Based on the equation, the P25 used in this study is 84% anatase and 16% rutile. After heating to 800°C, anatase peaks are no longer observed indicating a complete conversion to the rutile phase.

The XRD spectra of CNT/TiO₂ and ZnO/TiO₂ compounds are shown in Figure 2-2 and Figure 2-3. The spectra show that the CNTs suppress the rutile formation. Only the anatase phase is observed in the CNT/TiO₂ material. The ZnO/TiO₂ particles contain both anatase and rutile phases as well as ZnO. The proportion of each phase was calculated to be 34 % anatase, 41 % rutile, and 25 % ZnO. The SrTiO₃ 20 % La doped electrospun nanorods follow the expected XRD pattern for SrTiO₃, as shown in Figure 2-4[173].

Grain size was determined from the Scherrer equation, Equation 2-2. K is the shape factor, 0.89, λ is the X-ray wavelength, β is the full width at half maximum, and θ is the Bragg angle. The grain sizes are reported as the average of the three highest intensity peaks of each phase from the XRD spectra.

$$Grain\ size = \frac{K\lambda}{\beta \cos(\theta)} \quad (2-2)$$

Figure 2-5 shows the grain sizes calculated from the Scherrer equation. The grain sizes are reported for the three highest peaks for each phase. The first two peaks are for the anatase and rutile peaks in the as-received P25, while the third peak

represents the heat treated sample that exhibits only the rutile phase. The high temperatures needed to convert anatase to rutile explain the slightly larger grain size in the pure rutile system. Differences in porosity of the materials, agglomeration, and aggregation account for the variations in surface area. The increased grain size of the heat treated samples leads to a substantial decrease in surface area as seen in Figure 2-6.

Figure 2-7 shows SEM images of the photocatalytic materials used in this work. P25, in Figure A exists as much smaller particle clusters than is apparent in the other images. However, sonication prior to conducting photocatalytic studies further separates the particles prior to photocatalytic testing. The observed agglomeration of these materials corresponds with the lower surface area observed in the non P25 materials Figure 2-8 shows TEM images of P25 and rutile particles. The photocatalysts typically exist as small clusters of roughly spherical particles.

The electrospun nanorods of SrTiO_3 : 20% La are shown in Figure 2-9. The high calcination temperatures caused the fibers to start to granulize; although, the fiber structure remains. The fibers have an average diameter of 158 ± 32 nm. This average was taken from the measurement of 20 fibers from different areas of the sample using ImageJ software. The fibers range in length from an estimated 0.5 to 2 μm . The rods themselves are made of much smaller grains as discussed in the following sections.

In order to better understand the extent of aggregation in the various materials, it is useful to compare the grain size and surface area. Assuming perfectly spherical grains, an estimate for the surface area based on the average grain size from the Scherrer equation can be determined. The grain size data are reported in Table 2-1

along with the BET surface area measurements for each material. In each case, the reported surface area is less than the grain size predicts. Particle agglomeration is likely the largest factor in the difference between these two values. Some of the difference is also likely due to error in the measurements and assumptions made by the equations e.g. departure from sphericity. The data suggest that Rutile and ZnO/TiO₂ are more aggregated than the other material systems. Sintering between particles caused by the higher temperatures needed to synthesis these materials is the likely cause.

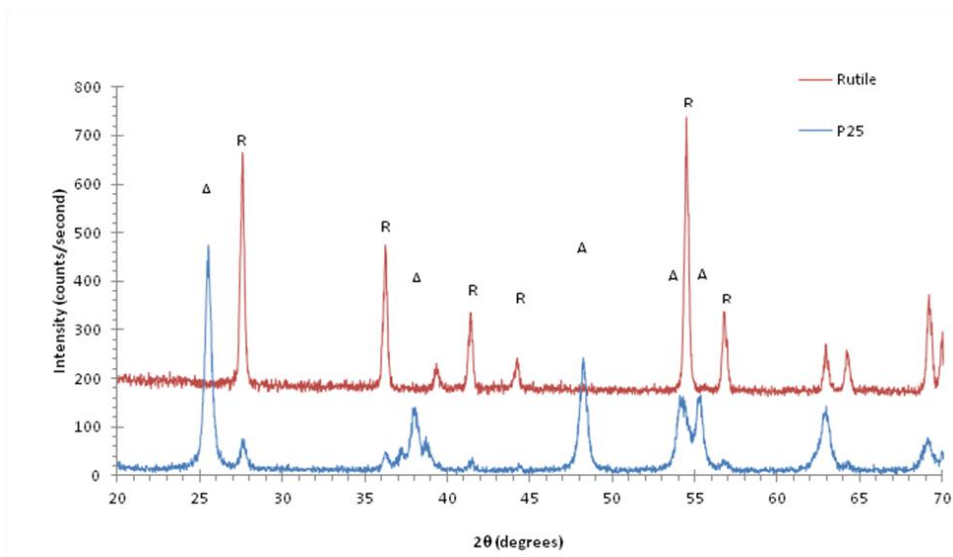


Figure 2-1. X-ray diffraction of P25 and rutile nanoparticles. Peaks labeled with “A” represent the anatase phase, while “R” peaks indicate the presence of the rutile phase.

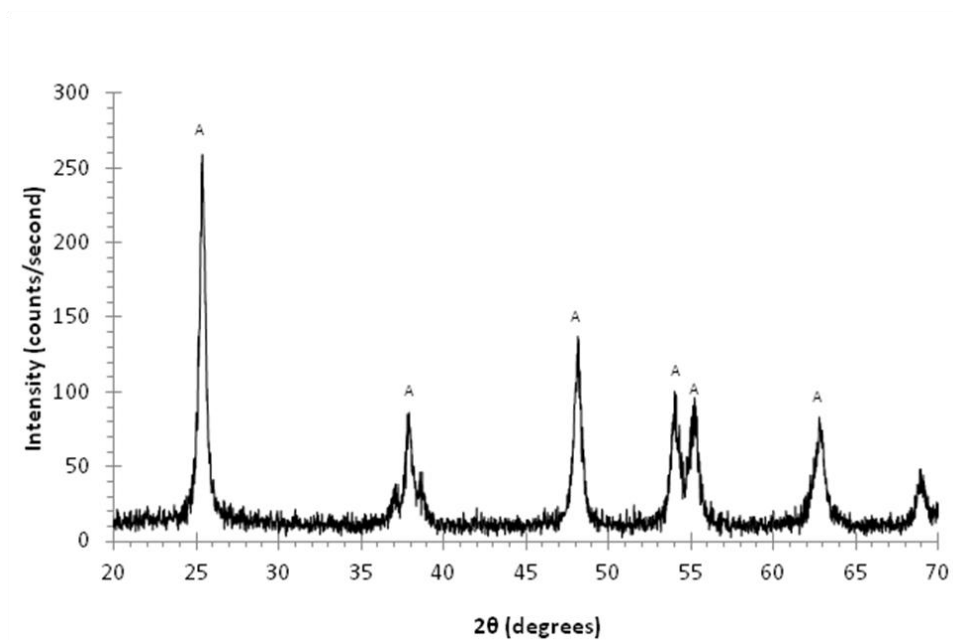


Figure 2-2. XRD spectrum of CNT/TiO₂ nanoparticles.

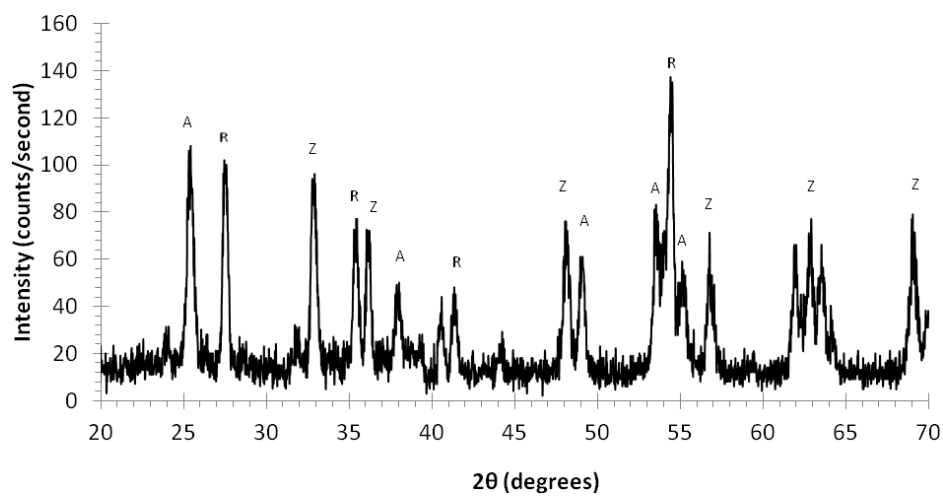


Figure 2-3. XRD spectrum of ZnO/TiO₂ nanoparticles. “A”, “R”, and “Z” represent the anatase, rutile, and ZnO peaks, respectively.

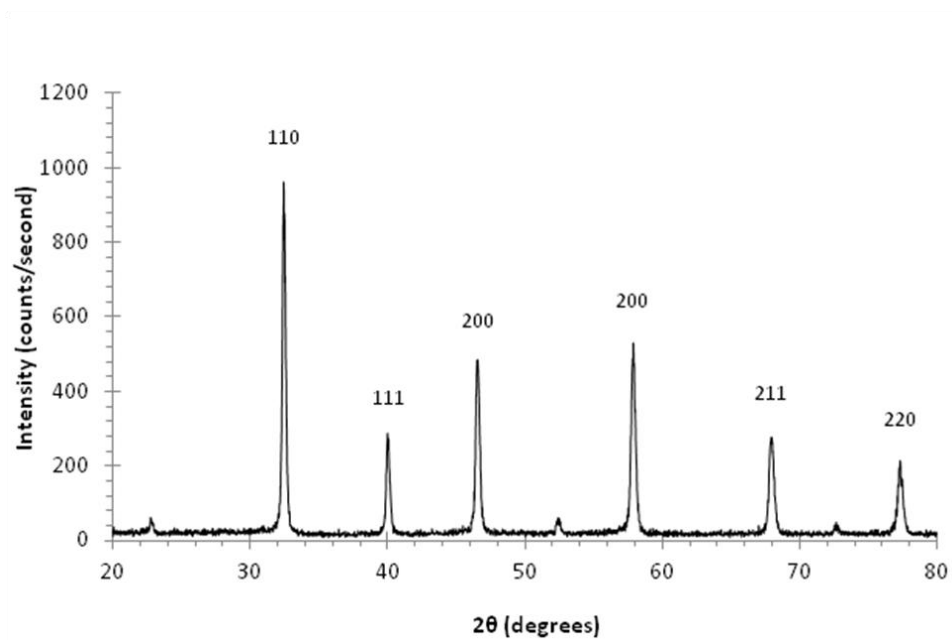


Figure 2-4. XRD of SrTiO₃: 20 % La electrospun nanorods.

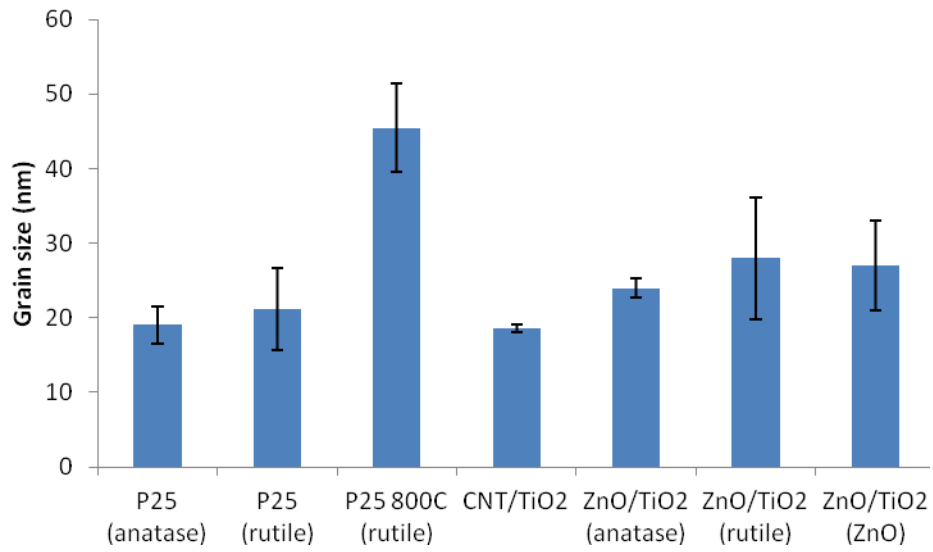


Figure 2-5. Grain size of photocatalytic materials reported from Scherrer equation.

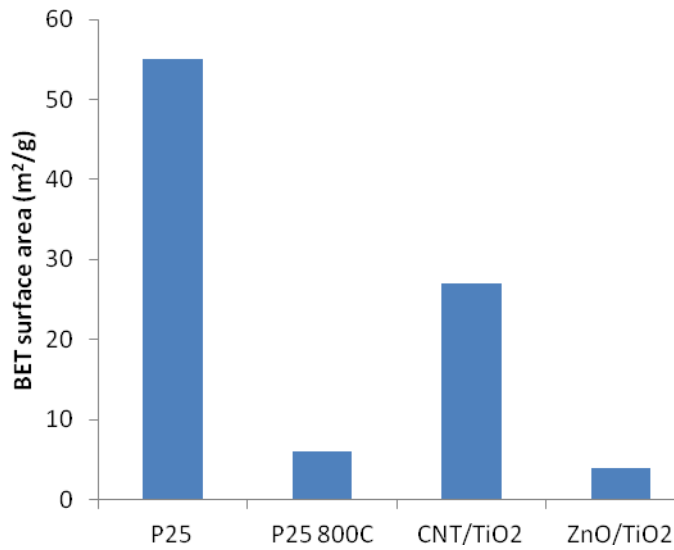


Figure 2-6. BET surface area measurements of photocatalytic materials.

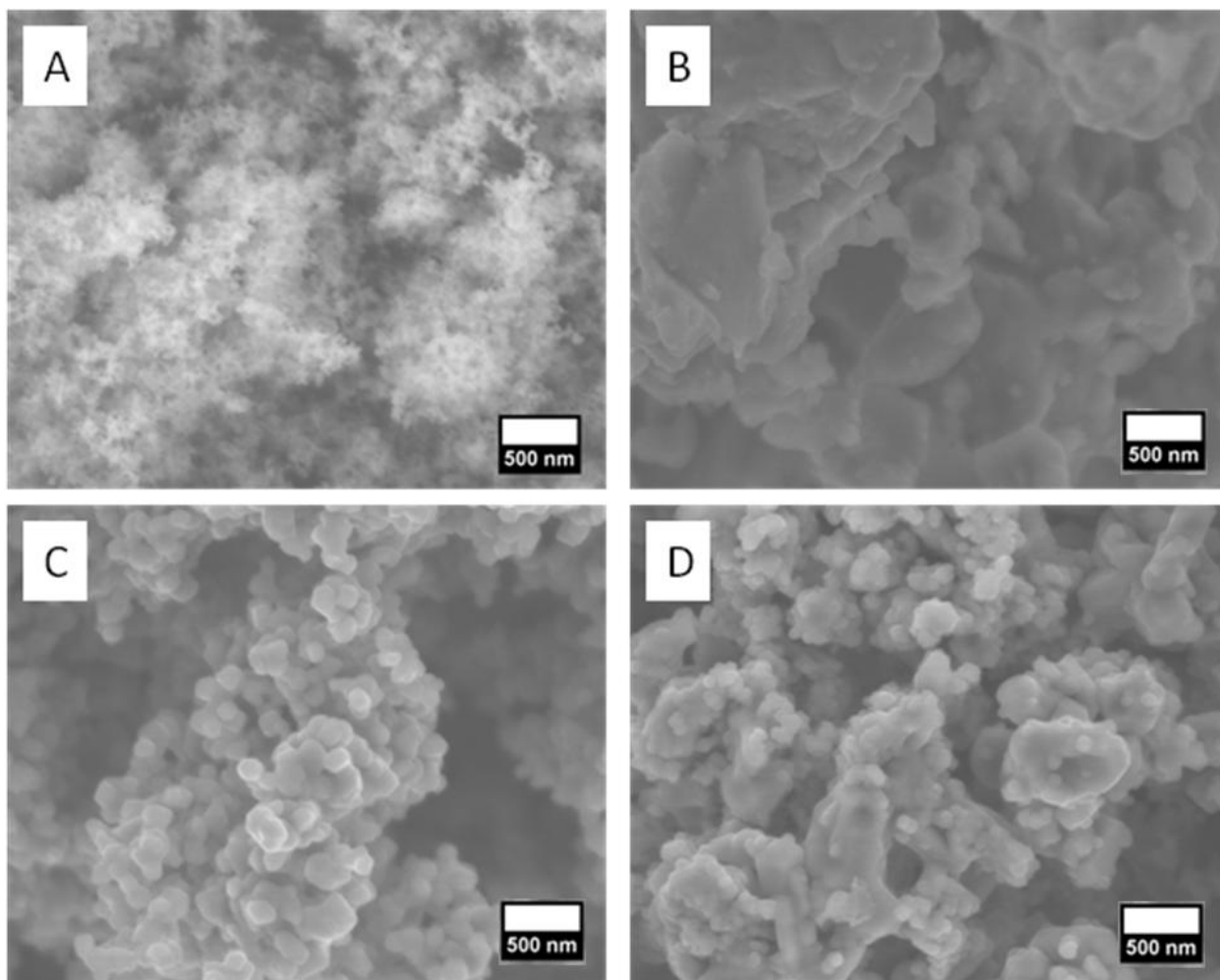


Figure 2-7. SEM images taken at the same scale of (A) P25 (B) CNT/TiO₂, (C) rutile, and (D) ZnO/TiO₂.

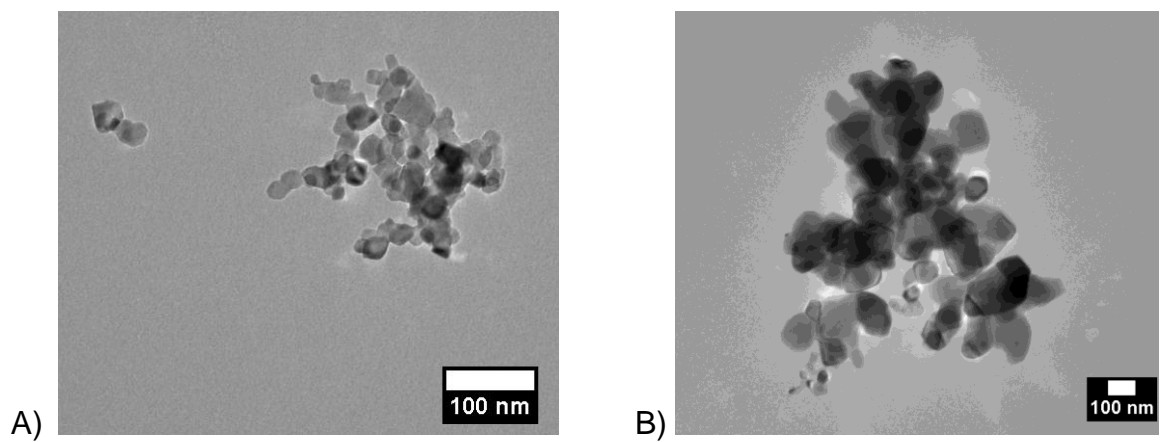


Figure 2-8. TEM images of (A) P25 particles and (B) rutile particles.

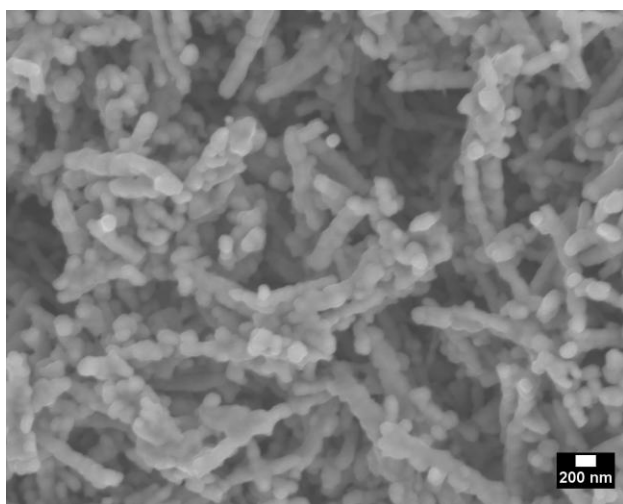


Figure 2-9. SEM image of SrTiO₃:20 % La nanofibers after calcination.

Table 2-1. Surface area predicted from Scherrer equation vs. BET measured surface area.

Photocatalyst	Predicted surface area (m ² /g)	BET surface area (m ² /g)
P25	70	55
Rutile	31	6
CNT/TiO ₂	85	27
ZnO/TiO ₂	50	4

CHAPTER 3 ELECTRIC FIELD EFFECTS ON PHOTOCATALYTIC ACTIVITY

Introduction

This chapter on the effects of electric fields on photocatalysis is divided into two parts. The first section discusses copper wires placed directly in the photocatalytic reactor, while the second section discusses the effects of placing the system inside a capacitor. The external capacitor setup was utilized due to effects of having the electrodes within the system. Specifically, deposition of particles on the electrode wires as well as decomposition of the wires themselves could influence the results. The electric field strength in the externally applied electrodes was only limited by sparking that occurred when the applied voltage was above 15 kV, which corresponds to an electric field strength of 2,300 V/cm. It should be noted that the photocatalytic activities between the two sections are not comparable due to slight changes in the reactor setup. In addition to the investigation of two different reaction setups, a range of common photocatalytic materials were tested. The following section describes the effects that are unique to each material system.

Materials and Methods

Throughout this work, the experiments are focused predominately on P25 and rutile. P25 is considered the standard with which photocatalyst experiments are compared to. Although the rutile phase is generally considered a poor photocatalyst, it is useful in that it is a single phase material. The separate phase regions in P25 help separate charge carriers. The internal charge separation might work synergistically or counterproductively with an external electric field. Therefore, it is useful to have a single phase material as a comparison.

Other photocatalytic materials have properties that might also have interesting performance in electric fields. CNT/TiO₂ photocatalysts are able to compete with P25 in terms of their photocatalytic activity depending on the synthesis route. As discussed in previous sections, the CNTs are able to efficiently shuttle away electrons. Since electron separation is highly efficient in this material, an external electric field might have less overall effect.

Electric fields might prove useful in systems that are not typically thought of as highly active photocatalysts. For example, in ZnO/TiO₂, it has been shown that charge transfer between the two phases is poor, but strongly improved by the presence of an electric field[112]. Such materials might undergo a greater performance increase than materials like P25. High aspect ratio materials might also prove interesting. The electric field might align the materials. The alignment of the materials might further improve charge separation. It was observed that pure TiO₂ nanorods had extremely low photocatalytic activity. However, SrTiO₃ doped with 20% La nanorods were highly active, and were used instead of the TiO₂ material.

Several factors were previously identified to affect the reported data in the photocatalytic testing process[174]. These include changes in lamp intensity and temperature of the system. However, the intensity and temperature appeared to reach a constant value. Therefore, the lamps in the photocatalytic system were turned on 30 minutes prior to conducting experiments. Samples were then run with and without the presence of an electric field with three replicates for each sample. The samples were randomly alternated between having the electric field active and deactivated.

Prior to running the experiments, the photocatalyst was sonicated in the dye solution for 15 minutes to disperse the particles. The material was then stirred in the dark to allow an adsorption/desorption equilibrium to be reached. The samples were then placed in an enclosed in a reaction chamber that prevented effects from external light sources and reflection of UV light that could alter the results between experiment runs.

The dye solution is very stable in the presence of both UV and visible light in the absence of photocatalytic material. Even after exposure to a UV-light source over the period of 90 minutes, no decrease in the concentration is observed[174]. The UV stability of this dye makes it an excellent model degradation product. Any decrease in intensity of the dye material must be due to degradation of the dye molecules or adsorption of the dye molecules onto the photocatalyst surface. Finally, separating the photocatalytic material from the dye solution was also critical. Typically, the material sedimented within 24 hours. After sedimentation, the dye solution was transferred to a cuvette for UV-vis. analysis. The materials were kept in the dark during the sedimentation process to prevent further degradation. As previously noted, the dye molecules themselves are able to drive a much slower reaction even when only visible light is present.

UV-Vis Absorbance Calibration Curve

Langmuir Hinshelwood kinetics requires an accurate measurement of the concentration of the dye material in the system. Figure 3-1 shows absorbance spectra of a dye solution at varying concentrations over the ranges used in the present study. The starting concentration of the dye used in all experiments in this study was 5 ppm.

The dye was observed to be very stable in UV light with no observable changes in absorption intensity after 18 hours in UV light.

The relationship between the relative absorbance and the concentration of the dye material is shown in Figure 3-2. The relative absorbance intensity corresponds directly with the changes in dye concentration with an R^2 value of 0.99. The linear relationship indicates that in the concentration ranges used in this study, changes in the relative absorbance intensity correspond directly with changes in dye concentration following the Beer-Lambert law.

Solution Conductivity

The conductivity of the DI water used was 5 $\mu\text{S}/\text{cm}$ the dye only slightly increased the conductivity to 8 $\mu\text{S}/\text{cm}$. The addition of P25 to the system did not alter the conductivity. In many studies, an electrolyte is added to the system, which is needed for photolysis of water, an effect that is ideally prevented in this study[175].

Copper Electrode Photocatalytic System

In the first set of experiments, copper electrodes were placed directly in the photocatalytic reaction chamber. The experiments were compared to a control with the same system with an applied electric field, but without the presence of UV light. This was necessary to ensure that the electric field alone did not affect the system due to the dissolution of copper that can occur or photolysis [176-177].

In order to determine the effect of copper dissolution and electric field on the system, a control experiment was run with dye material alone with a current and UV light applied. A reaction rate of $k_{\text{app}}=-0.0011 \text{ min}^{-1}$ was observed for the removal of dye from the system. The negative value of the reaction rate indicates an increase in dye concentration. An increase in concentration could be attributed to removal of water from

the system through either evaporation or electrolysis. The decrease in dye intensity is extremely small and likely within error of the measurements. The photocatalysts' tests were typically observed to have a reaction rate that is higher by an order of magnitude.

The electrodes were made of copper wires and separated by a distance of 5 cm. The electric field strength between the electrodes was calculated to be 4 V/cm with a current of 3 A. While electrolysis occurs in water above 1.2 V, the reaction requires an electrolyte to proceed at a rate that could influence the reaction. Figure 3-3 demonstrates the change in photocatalytic performance for P25. It was observed that both positive and negative applied voltages resulted in an improvement in photocatalytic performance. Both electrodes underwent a similar increase in performance. This study appears to have similar results to the improvement of thin film photocatalysts using an internal electrode system[111].

Conclusions

Copper electrodes can confer a performance increase on a dispersed P25 photocatalytic system in a similar way to which they increase performance in thin film systems. The copper electrode, electric field, and UV light alone do not appear to have a significant impact on the dye concentration. However, higher applied voltages will lead to electrolysis and degradation of the copper electrodes. Therefore additional studies were conducted using an external parallel plate setup as described in the following section.

Parallel Plate Electric Field Setup

In order to apply higher electric field strengths while mitigating the effects of electrolysis and electrode dissolution, an external electric field setup is used in the following studies. A schematic of the setup is shown in Figure 3-4. UV light is emitted

from overhead lights, while a stir bar maintains particle dispersion and prevents diffusion from limiting the reaction rate. A parallel plate capacitor is built outside of the reaction container. The plate was assembled from aluminum foil with a separation distance of 6.5 cm. The electric field strengths reported here are reported through air and not adjusted for internal effects as it passes through the system. The maximum applied electric field strength of 2300 V/cm was limited by sparking that begins to appear when higher voltages were applied.

Particle Motion in an Electric Field

The electric field is expected to accelerate the nanoparticles linearly, which could influence their dispersion and sedimentation rate. Excessive buildup of the nanoparticles on one wall of the container could significantly alter photocatalytic performance. However, this effect is mitigated in the following experiments since the containers are under constant stirring. In this first set of experiments a setup without a stirbar was used in order to better examine the effects of an electric field on the system.

P25 in dye solution (3 mg/50 mL) was placed inside an electric field without stirring in a transparent container with a control sample placed outside of the electric field. After 24 hours the samples were examined. In both cases, the particles were no longer dispersed in the system, and all dye had been degraded even without the aid of UV light sources. In both cases, the majority of the material sedimented to the bottom of the cuvette.

Figure 3-5 shows optical darkfield images of the containers. The two images can be interpreted as follows. The left image is of a container that was placed in an electric field. In this image, particles deposited on the wall of one side of the container. This can be observed by the hazy striations that appear. This coating on the walls is absent from

the image on the right. Although only present in the photo on the right, both containers had large particle aggregates floating in solution. These aggregates were likely agitated when the containers were tilted onto the microscope.

To prevent the deposition observed in this model system, the photocatalytic reactor used in the follow experiments was subjected to stirring. No noticeable preferential buildup on any side of the container. This agrees with previous studies on viscous forces of TiO_2 particles in electric fields discussed in previous sections.

Electric Field and UV Effect on Procion Red Dye

The photocatalytic system was first tested in the absence of P25 particles. This experiment was conducted to ensure that the electric field alone did not affect the degradation of the dye molecules or significantly alter their surface adsorption. There were no apparent changes in concentration over the period of one hour. This indicates that over the time periods used in the subsequent studies, the dye material should be unaffected by both the electric field and UV light.

Electric Field Effects on a P25 Photocatalytic System

Several materials were investigated in the presence of an external electric field. This first section will focus on P25, while subsequent sections will discuss the effects observed in other materials. A range of electric field strengths were applied to the system in order to determine how the performance changes with changes in electric field strength. Figure 3-6 shows the rate constants that were observed over a range of electric field strengths. This image clearly shows that the photocatalytic performance increases with the electric field strength. The rate constant increased by 120 % with an

applied electric field of 2300 V/cm. This corresponds with removing the dye from the system 55 % faster than in the absence of an electric field.

There are several potential ways in which an electric field can influence photocatalytic ability as outline in the background section. Three likely possibilities of enhancement in photocatalysis are: improvement in dye adsorption on the TiO₂ surface, enhanced particle dispersion and motion, or improvement in charge transport within and between the particles. The first two possibilities do not appear to have a major influence. The dye concentration does not appear to change when placed in the dark with P25 in the presence of an electric field alone. The second case of particle acceleration also does not appear to be a major factor. As previously discussed the viscous forces created by a stir bar are expected to overcome the effects of any electrophoretic motion. Therefore, the most likely explanation is an increase in the internal charge carrier transport.

Electric field studies on TiO₂ thin films in the literature suggest that the Poole-Frenkel mechanism is responsible for improvements in photovoltage. Therefore, it is reasonable to assume that in the current photocatalytic reaction, a similar effect is predominantly responsible for the enhanced photocatalytic performance. Since the increase in conductivity in the Poole-Frenkel effect is related to the release of trapped charge carriers, it is reasonable to assume that the increase in photocatalytic performance would follow the same trend if a similar mechanism is the primary driving force in the effect. Therefore, if this is the predominate effect, the improvement in performance of photocatalytic activity should follow a similar form to the Poole-Frenkel model. A plot of the natural log of k_{app} vs. the square root of the applied electric field

should result in a straight line. This plot is demonstrated in Figure 3-7, and shows an R^2 value of 0.93, indicating a reasonably good fit, given the degree of variability in the data set.

The obtained slope can then be substituted back into the Poole-Frenkel equation to create a model for the system as shown in Figure 3-8. The model has an R^2 value of 0.94. This trend predicts a gradual leveling off in the improvement that occurs with increases in electric field strengths. The model is useful for predicting how the photocatalytic increases might continue with further increases in the electric field.

Electric Field Effects on Rutile, CNT/TiO₂, ZnO/TiO₂

The photocatalytic performance of several other systems in the presence of an electric field was also tested for Rutile, CNT/TiO₂, ZnO/TiO₂. In these studies only the data with and without an applied electric field of 2300 V/cm is reported. This field strength is the highest that could be applied to the present system.

The data for P25, rutile, CNT/TiO₂, and ZnO/TiO₂ systems is shown in Figure 3-9. The data show that the reactivity of the materials on a mass basis is P25>ZnO/TiO₂>CNT/TiO₂>rutile. The increase in performance in the presence of an electric field appears to follow a different trend as follows: P25>CNT/TiO₂>rutile>ZnO/TiO₂. However, it should be noted that the error bars of several of these materials overlap, indicating that some of these materials likely underwent similar improvements in performance. This information is better visualized by Figure 3-11. Interestingly, the BET surface area follows the same trend with the greater improvements in performance seen in the materials with the highest surface areas. However, these materials are complex, and a number of factors likely affect the systems.

Instead of reporting the reactivity on the basis of the mass of the photocatalyst used, it is possible to normalize the data based on surface area, as reported in Figure 3-10. This second graph allows the reader to better understand how active the surfaces of these materials are despite the differences in particle size. In this case the reactivity of the materials changes to ZnO/TiO₂>rutile>P25>CNT/TiO₂. However, the normalization does not alter the change in improvement due to an electric field.

There are several possible reasons for the differences in performance increases in the electric field. These possibilities include:

1. The Poole-Frenkel effect is material dependent. It is possible that charge carriers in P25 are more easily influenced than the other systems. With higher applied electric fields, a similar trend may be observed in the other systems.
2. Several of the systems have internal electric fields that help separate charge carriers. Therefore, the internal electric field may have already been efficiently separating charge carriers, resulting in a smaller improvement from the external electric field. Conversely, the separation might act synergistically with the electric field allow charge carriers to be more easily separated.
3. The internal electric fields between particles and between the composite systems may act in a competing effect with the external electric field lessening its overall effect.
4. The improvement in performance follows the trend of higher improvement in performance with materials with higher surface areas. It is likely that aggregated and larger particle sized materials also see improvement in charge transport, but most of the charge carriers end up recombining in the bulk.

Photocatalytic Nanorods in an Electric Field

Electrospun photocatalytic compounds can be used directly as supported catalyst systems. However, these highly porous films differ significantly in reaction rate when reused due to the effects of adsorption, possible loss of material, and catalyst fouling. Therefore, the fibrous meshes were ground into nanorods for this part of the study so the influence of the electric field on the nanorods could be determined. The

dispersed particles also have significantly faster reaction rates since diffusion of reactants to the surface is greatly increased.

High aspect ratio photocatalytic materials might demonstrate unusual effects in the when exposed to an electric field. The shape of these particles might give rise to dipoles that orient the system in ways that nanoparticles themselves do not undergo. The nanorods were prepared through an electrospinning process. The resulting fibers were heat treated and ground to form nanorods. Electrospun TiO₂ nanorods with diameters on the order of 100 nm were observed to have extremely poor photocatalytic performance and could not be used for this experiment. On the other hand, doped nanorods were slightly more active than rutile K_{app} of 0.004 and 0.003 for SrTiO₃:La nanorods and rutile, respectively. The improvement in performance due to an electric field was 58 ± 22 %, which is second only to the improvement of P25. The rate constants with and without an electric field are shown in Figure 3-12.

Conclusions

Application of electric fields to photocatalytic systems improved the photocatalytic reaction rates in all of the systems tested. The improvement in performance depends strongly on the material. P25, and SrTiO₃: 20 % La had the largest improvements in their rate constants at 120 % and 58 %, respectively. CNT/TiO₂, ZnO/TiO₂, and rutile were observed to only have modest improvements in performance. P25 was observed to increase in photocatalytic performance with electric field strength. The increase followed similar trends to charge carrier transport increases in thin film TiO₂ materials, which suggests a similar mechanism is responsible in the present systems. There also appeared to be a dependence on the surface area of the material, indicating the recombination in the bulk is likely a limiting factor.

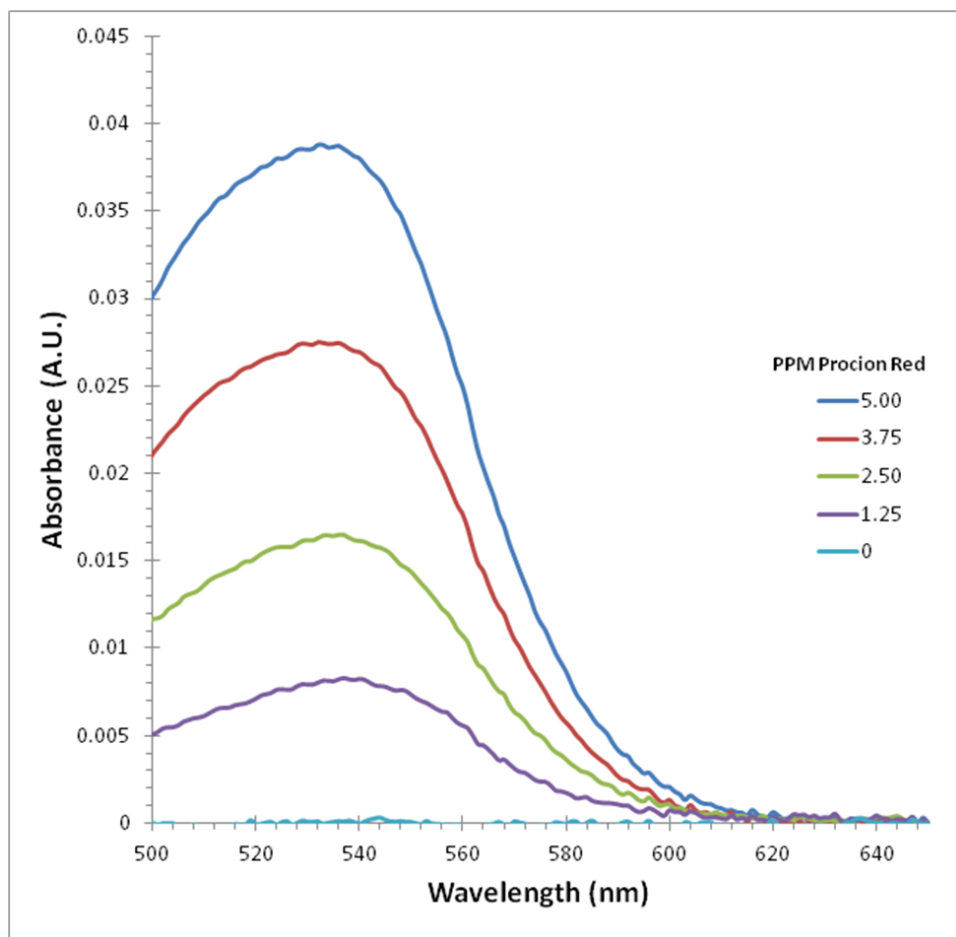


Figure 3-1. Absorbance curves of varying concentrations of Procion Red dye.

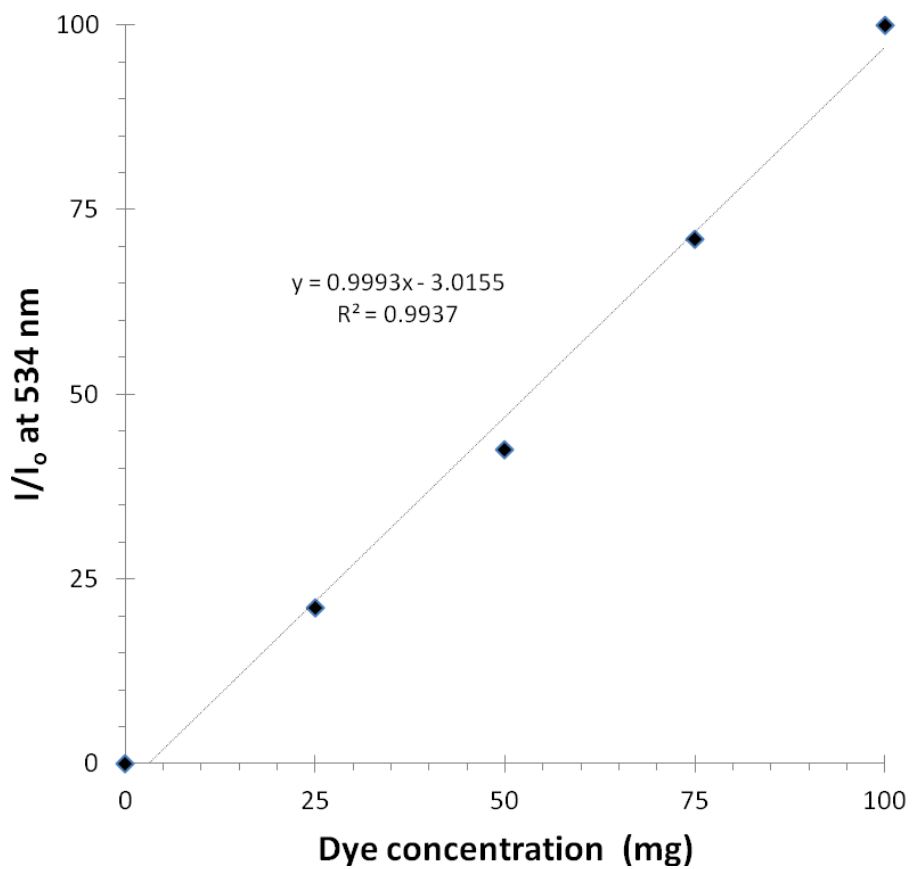


Figure 3-2. Intensity vs. concentration of Procion Red dye.

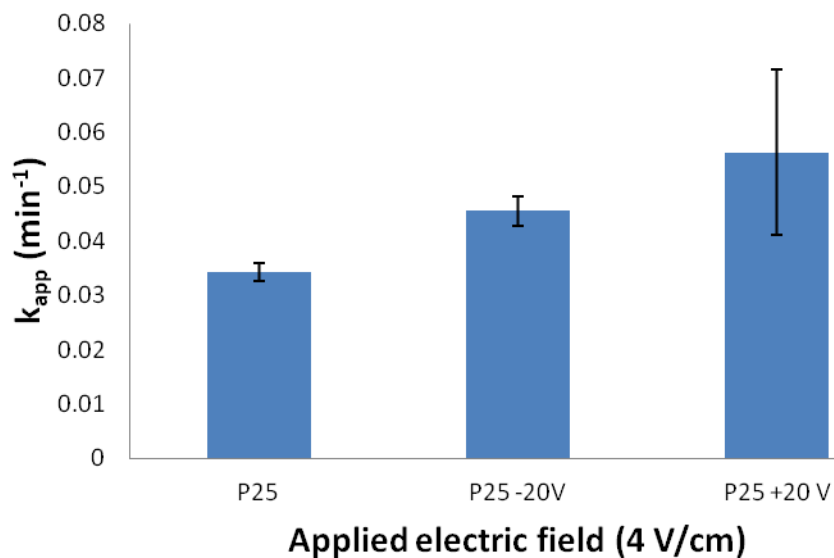


Figure 3-3. Electric field enhancement using copper electrodes.

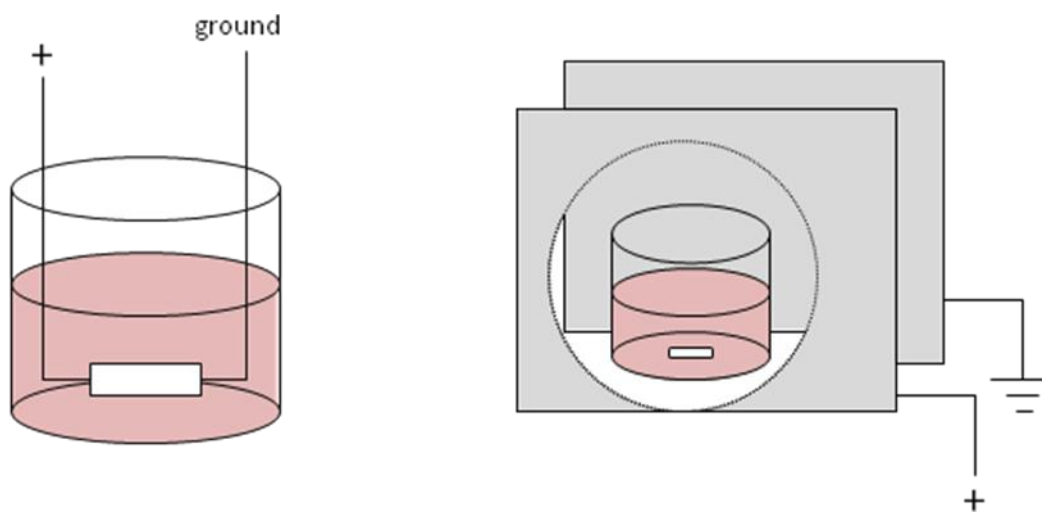


Figure 3-4. Types of photocatalytic reactors. Left: Typical supported photocatalysis system with electrodes inside the reaction vessel connected to a thin film. Right: External parallel plates with cutaway image showing the reaction vessel in between. The white bar represents a stir bar in the system.

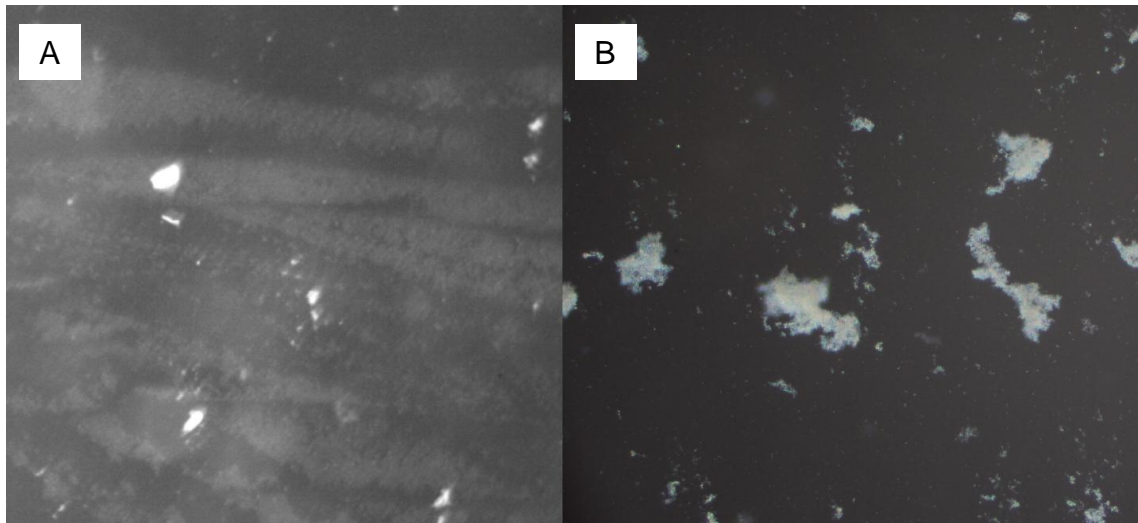


Figure 3-5. Particle deposition on containers walls in an electric field. Darkfield microscopy at 5X magnification of container side walls after 24 hours of sedimentation in (A) an external electric field, and (B) without an applied field. Photo credit: Michael Laudenslager.

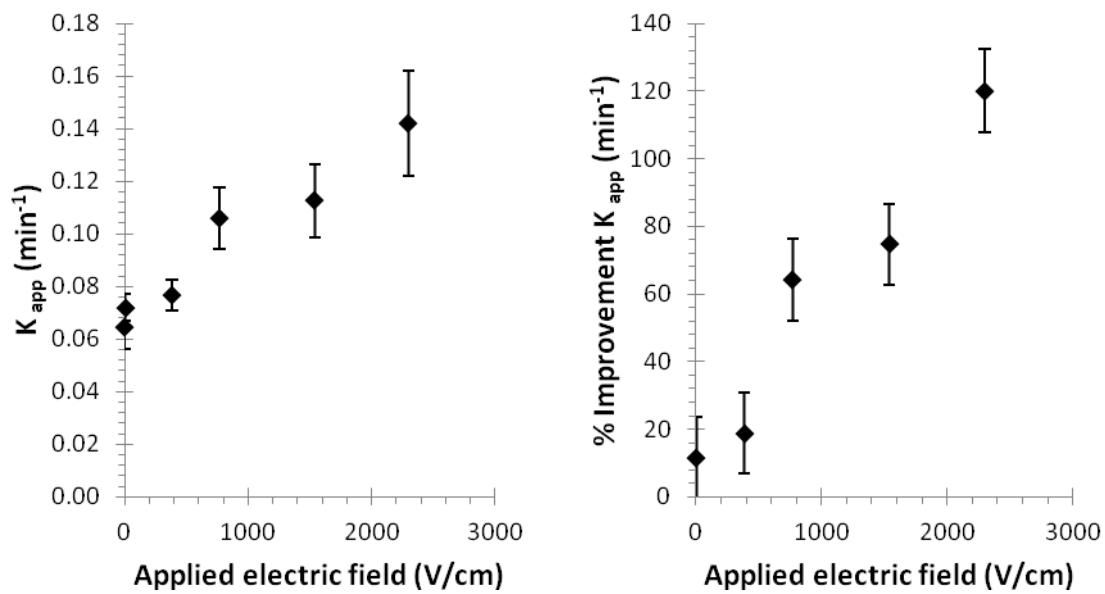


Figure 3-6. Left: Rate constants of P25 in the presence of varying electric field strengths
 Right: Improvement percentage in rate constant with electric field strength.

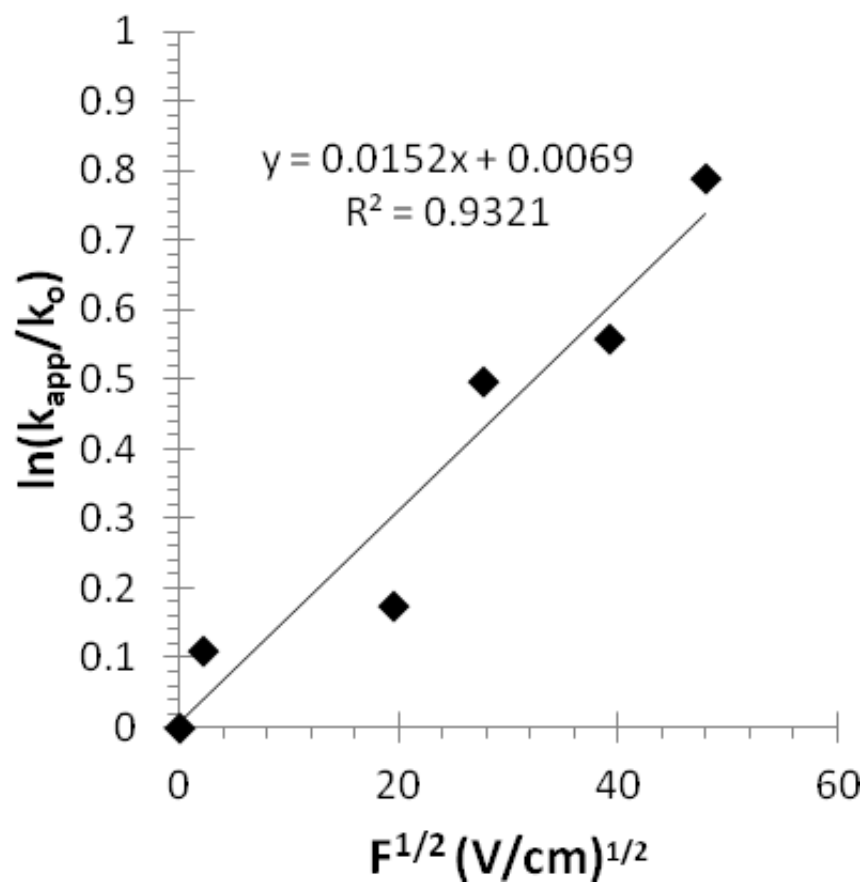


Figure 3-7. Natural log of rate constant vs. square root of electric field strength.

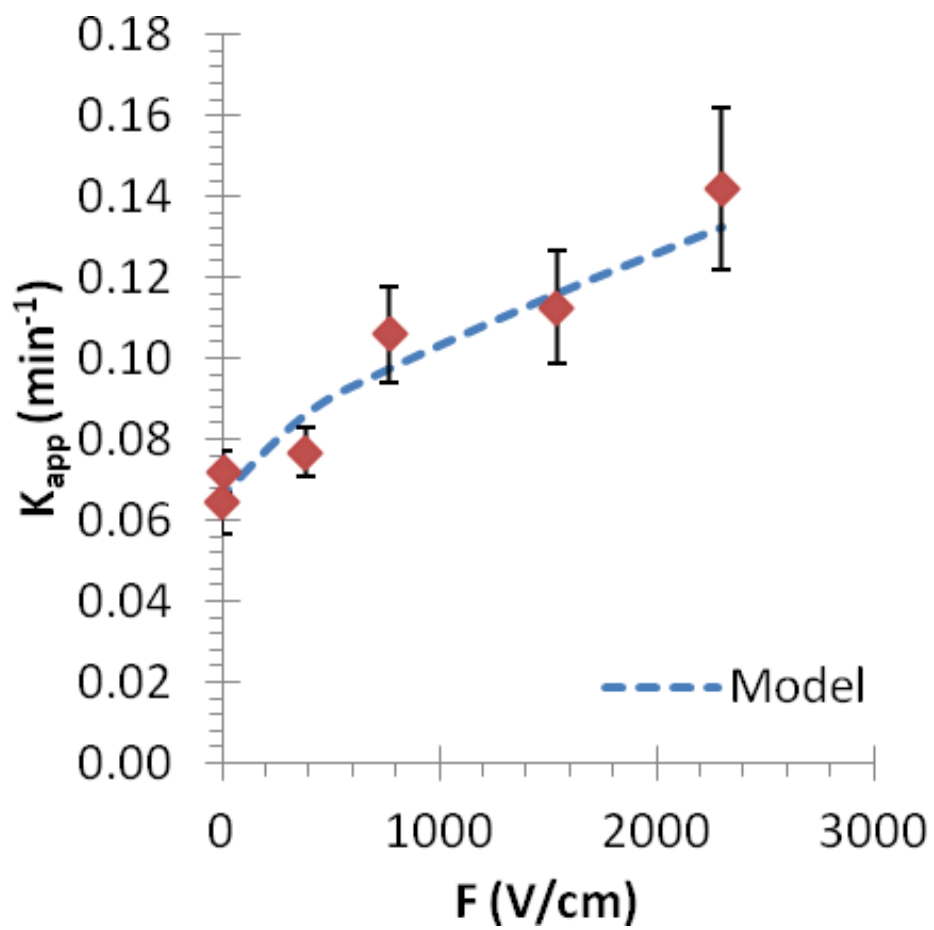


Figure 3-8. Fitted equation based on Poole-Frenkel model.

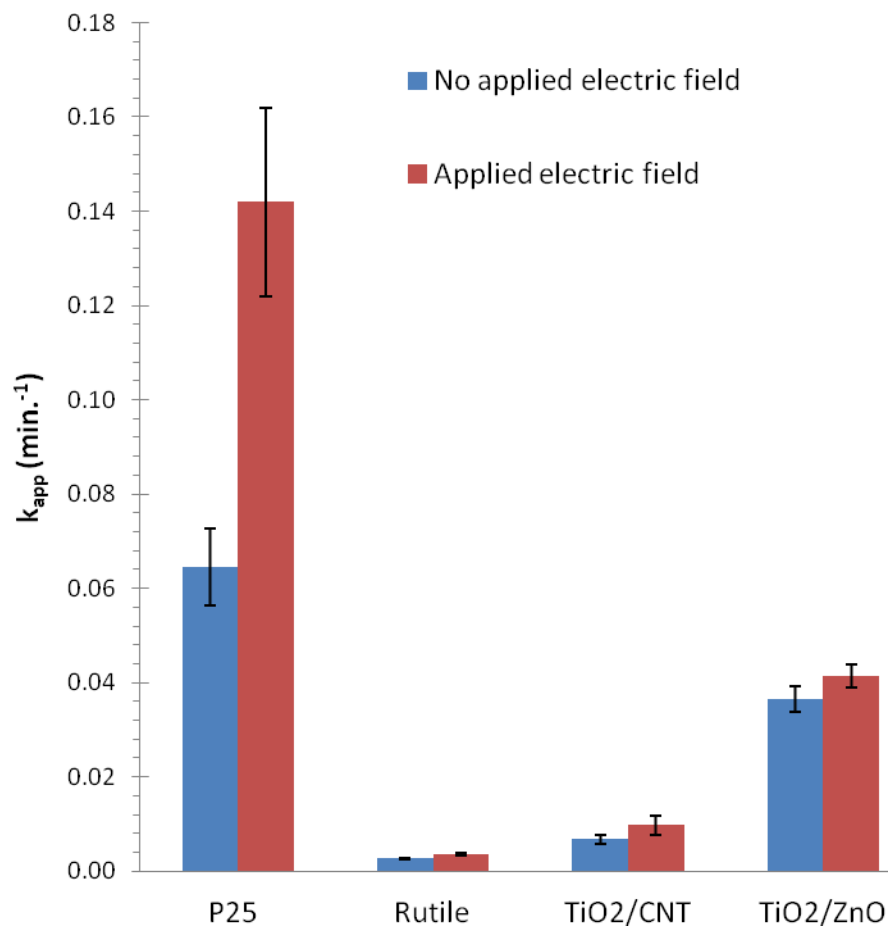


Figure 3-9. Photocatalytic performance without an applied electric field and with an applied electric field of 2300 V/cm.

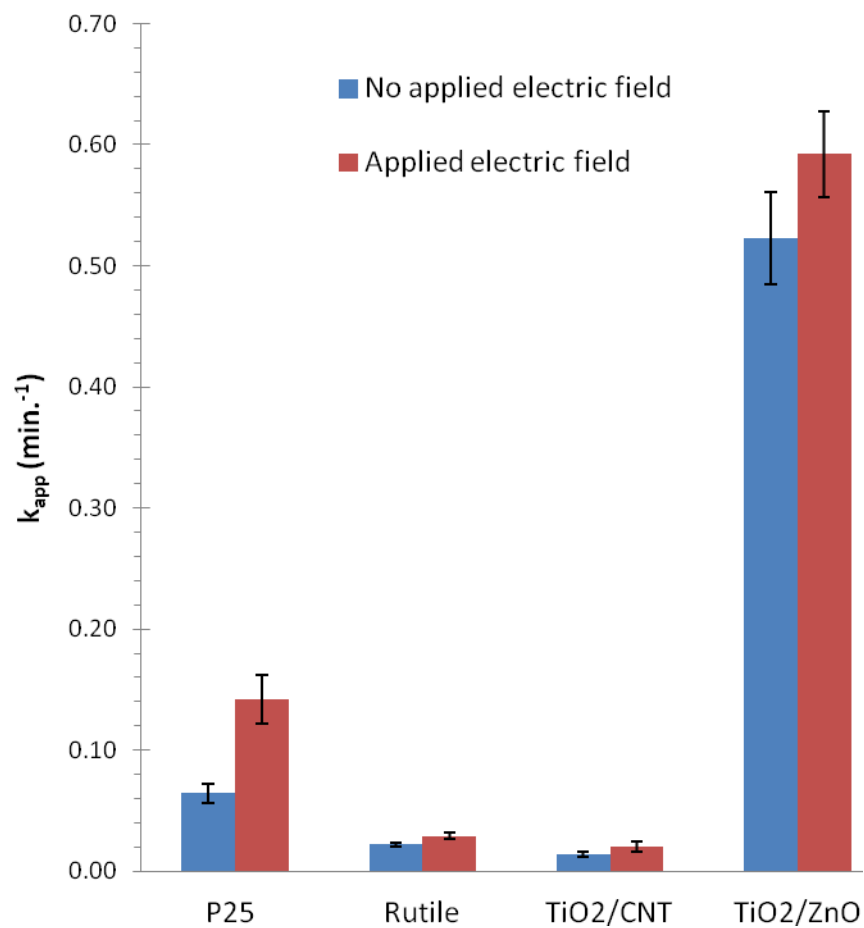


Figure 3-10. Photocatalytic performance without an applied electric field and with an applied electric field of 2300 V/cm normalized for surface area.

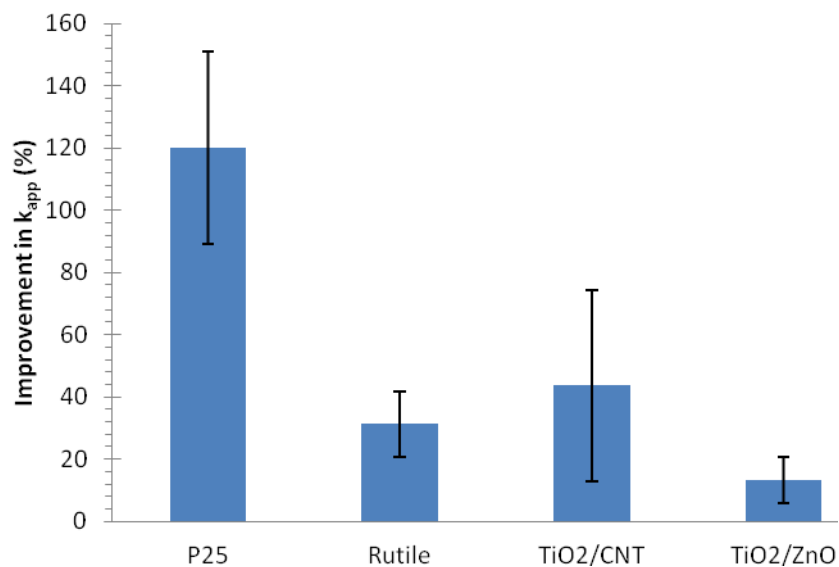


Figure 3-11. Percentage improvement in k_{app} at 2300 V/cm over k_{app} without an applied electric field.

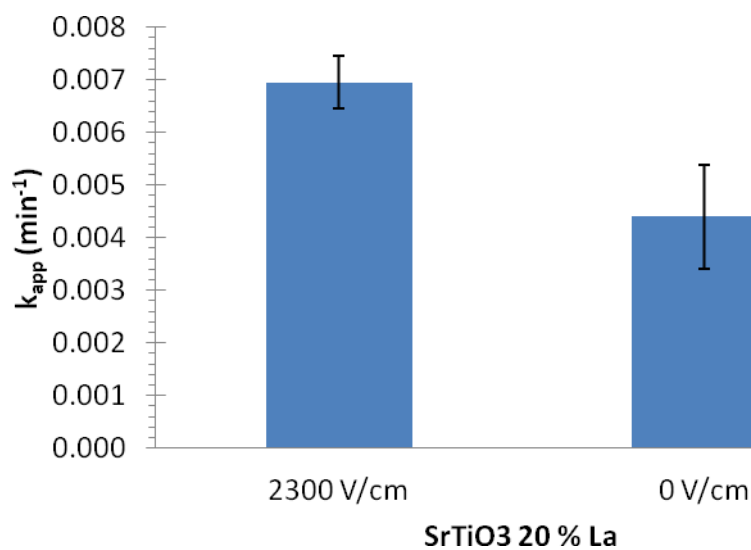


Figure 3-12. Reaction rates of SrTiO₃ with and without an applied electric field.

CHAPTER 4 LIGHT INTERACTION WITH PHOTOCATALYTIC SYSTEMS

Introduction

Determining how light interacts with the photocatalytic system is essential to developing an efficient reaction setup. Light is absorbed and dispersed as it passes through the dispersed nanoparticle system. TiO₂ nanoparticles strongly scatter visible light, while absorbing light with energy greater than their bandgaps. Rutile has a bandgap of 3.0 eV while anatase has a slightly higher bandgap of 3.2 eV. The bandgaps correspond to 413 and 388 nm, respectively. The following section discusses how far light travels through the current system, which gives insight into the size limitations of reaction setups.

Since various compounds are degraded by photocatalysts, the light interaction with the dye material is excluded from this study. Additionally, the dye concentration is not constant so it is more useful to determine the interaction with the photocatalyst dispersed in water only. Furthermore, the dye material is transparent in the UV range and should not significantly affect the absorbance in the range that the P25 particles absorb.

Light Extinction through Dispersed Particles in Liquid

In order to determine how light interacts with the present system, P25 was dispersed in DI water. Figure 4-1 shows the transmission of light at varying wavelengths through a cuvette with an optical path length of 1 cm with dispersed P25 particles. All of the experiments conducted in this study were performed with the same concentration of photocatalyst to water used in the previous experiments (6×10^{-5} g/mL P25/DI water). In

this figure, it is clear that above 400 nm, less than 20 % of light is transmitted. This value drops to nearly zero transmission at 340 nm and above.

It is important to note that Figure 4-1 does not differentiate between light that is scattered and light that is absorbed. The important information that can be gained from this study is that in a reactor system with this particle concentration, the majority of UV light is attenuated after it travels through 1 cm of the system. Therefore, a shallow photocatalytic reactor with the same volume of fluid would have significantly higher reported photocatalytic performance than a narrower, deeper container.

In order to determine the relationship between particle concentration in the fluid and transmittance through the system, the transmittance data at 380 nm was plotted in Figure 4-2. The light absorption vs. particle concentration has a linear relationship with an R^2 value of 0.98. This relationship was observed to hold true for higher and lower wavelengths.

From this information it is possible to determine the portion of the reaction container that is used in this study that is in the highly active photocatalytic region. Since Pyrex glass blocks UV light, it can be assumed that light only enters the system from the top of the reaction chamber. The liquid in the container has a height of approximately 3 cm and a radius of 2.5 cm. Therefore, only 33 % of the total sample is in the highly active region.

Conclusions

Light attenuation through photocatalytic systems imposes limitations on reactor design. P25 particles strongly absorb and reflect light. By having a general understanding of how light interacts with such a system, future experiments can be designed accordingly. P25 particles can only absorb UV light with wavelengths less

than 413 nm. At 413 nm only 20 % of incident light on a system makes it past the first centimeter of particles dispersed in water. Although, there is a strong wavelength dependence, a rough estimate of the region that is highly active in the present study indicates that light in the UV range (305 nm) only strongly interact with about 33 % of the sample. Overall, these results indicate that building a reactor that is more than a few centimeters in depth is not necessary, and will appear to have a slower reaction time than a shallower container.

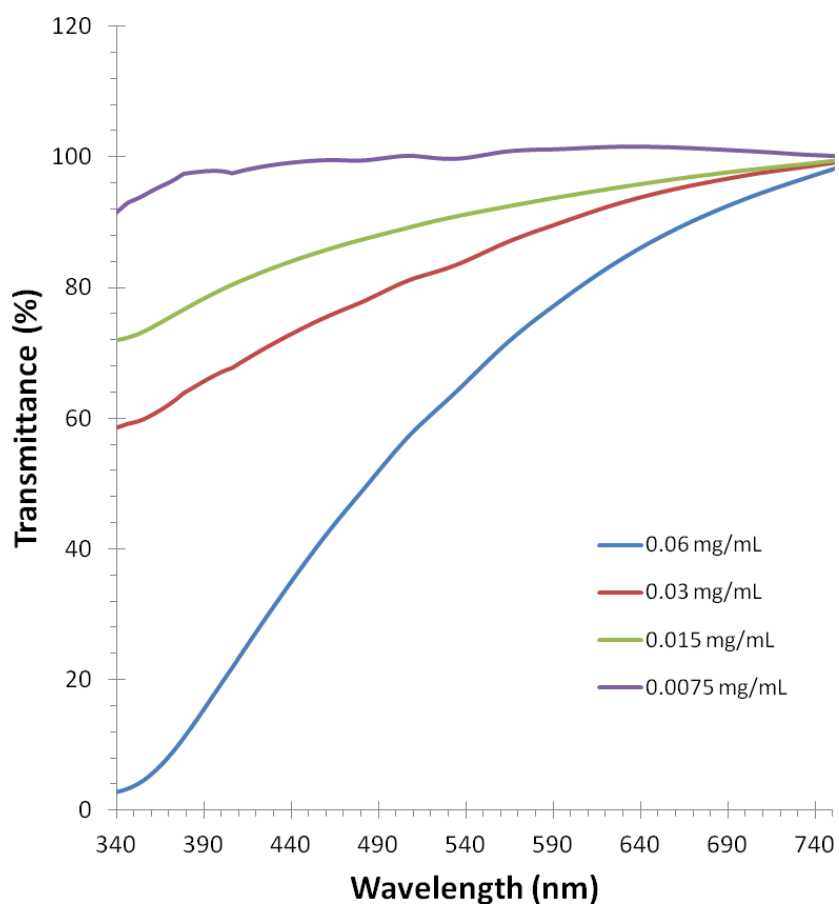


Figure 4-1. Transmittance of varying quantities of P25 dispersed in DI water through a cuvette with an optical path length of 1 cm. The present work had a dye concentration of 0.06 mg/mL.

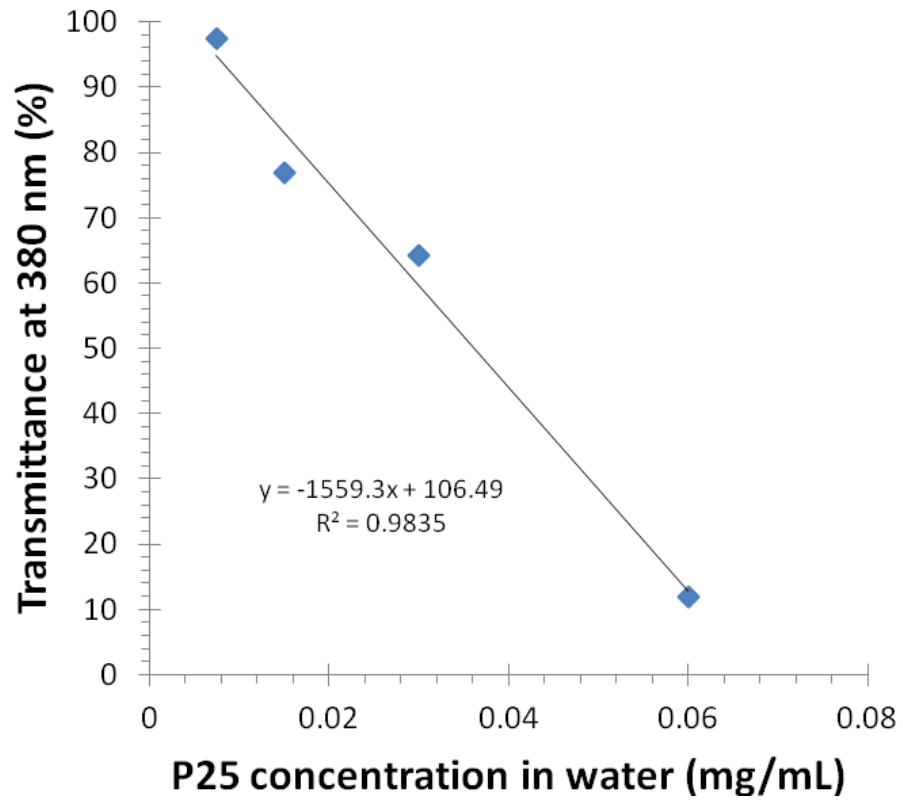


Figure 4-2. Transmittance at 380 nm vs. P25 concentration in water.

CHAPTER 5

ELECTROSPINNING OF HIGH CONDUCTIVITY SOLUTIONS

Introduction

Electrospun fibers can be used as catalysts support materials due to their high porosity. There are two methods that electrospun fibers can be used in supported photocatalysts. It is possible to embed catalyst material directly into the fibers or to develop a highly porous mesh of the catalyst material itself[51-52] [53-54]. While supported catalysts have significantly lower activity than dispersed particle systems, the systems have the advantage of allowing the catalyst material to be readily removed from the system.

Electrospun materials typically deposit on the collection surface as flat sheets of porous nanofibers. However, ceramic and composite systems require precursor solutions that have high conductivities. The high conductivity gives rise to new behaviors that are not reported elsewhere. Although previous studies have reported electrospinning precursor solutions with high conductivity (10,500 -21,645 uS/cm), the departure from the standard electrospinning process has not been previously discussed[167, 178]. The previous studies on high conductivity electrospinning solutions only collected a small number of fibers. The short electrospinning times were likely not long enough to observe the departure from the standard electrospinning process reported here.

Materials and Methods

TiO₂ precursor solutions were prepared containing varying quantities of NaCl to alter the solution conductivity. These solutions were prepared as follows. Acetyl acetone (1.5 g) was added to ethanol (4 mL) prior to the addition of titanium isopropoxide (1.5 g).

Polyvinyl pyrrolidone (0.5 g) was then dissolved in the solution. In a separate container, concentrations of NaCl, listed in Table 5-1, were added to DI water (4 mL). Upon complete dissolution of the NaCl, the salt solution was stirred into the titanium isopropoxide solution.

SrTiO₃ doped with 20 % lanthanum was electrospun from the following formulation. DMF (12 mL), PVP (0.83 g), and titanium isopropoxide (0.53 g) were mixed in a container. In a separate container, strontium nitrate (0.6 g), and lanthanum (III) nitrate hexahydrate (0.14 g), and water (2 mL) were prepared. After complete dissolution, both solutions were combined. All solutions were electrospun at a voltage of (+20 kV) with a distance of 20 cm between the tip of the needle and the collection plate at ambient temperature. The flow rate was kept at a constant 0.5 mL/hr. The electrospun fibers were collected on grounded aluminum foil.

Solution Conductivity

In order to understand the effect of conductivity on the system, several ceramic precursor systems were prepared with varying conductivities. Both the shape of the collector and the conductivity were observed to influence the fiber morphology. In the first set of experiments, a circular collection plate was used with a titanium dioxide precursor solution. The conductivity was varied by the addition of NaCl. Table 5-1 summarizes the observed fiber morphology with changes in solution conductivity due to the addition of NaCl. The concentration of NaCl could not be increased further without precipitating from the precursor system.

At low conductivities, the fibers deposited as a flat mesh. This flat mesh structure is typical for electrospinning, and shown in Figure 5-1. As the conductivity increased to

1270 $\mu\text{S}/\text{cm}$ and higher, the fibers began to collect preferentially along the edges of the collection plate. The fibers appeared to form a web-like pattern as shown in Figure 5-2 and Figure 5-3. As the conductivity increased further, the effect changed the morphology of the collected fibers. At the highest conductivity, 2,800 $\mu\text{S}/\text{cm}$, the fibers attached perpendicularly to the collection plate. These fibers formed thin sheets in the center of the collection plate that periodically collapsed outward. This resulted in a corolla-like structure, shown in Figure 5-3.

Influence of Collector Shape

In a typical electrospinning process, the collector dimensions do not have a significant impact on fiber morphology. However, as the conductivity is increased, the shape of the collector was observed to have a significant impact on the morphology of the collected fibers. The previous set of studies were conducted with a collector with a diameter of 8 cm. It was observed that either increase or decreasing the collector size resulted to a change in the morphology of the collected fibers.

A series of experiments were conducted to determine the influence of collector shape on fibers with conductivities of 1500 $\mu\text{S}/\text{cm}$. Both smaller ($d=5$ cm) and larger collectors ($d=12$ cm) resulted in low density arrays of fibers once the critical solution conductivity had been reached. Instead of the “webbed” structures that were observed in the previous experiments ($d=8.5$ cm), these collectors resulted in “cotton ball” structures.

In the case of the 5 cm diameter collection plate, the fibers collect preferentially along the edges of the collector. This is initially similar to the effect of the 8.5 cm diameter collection plate. However, in this case, the webbed fibers collapse inward readily and build up as a low density structure. This structure is shown in Figure 5-4.

Increasing the size of the collector to diameters larger than 12 cm resulted in fibers collecting centrally from the grounded plate. These fibers formed cones that extended outward 10-15 cm from the collection plate, as seen in Figure 5-5. Periodically the cone will collapse due to instabilities in the electric field. The cone thins as it gets closer to the collector. The entire strand periodically bends inward forming loops in the collected structure, which are shown in Figure 5-6.

The three dimensional collector shape of the electrospun fibers continues to extend outward over time. If this structure is allowed to extend too far, it will interfere with the electrospinning process. As the structure approaches the needle, liquid droplets have an increasing tendency to be ejected, which destroys the structure of any fibers that come into contact with the drop. However, it is possible to avoid this structure altogether by electrospinning onto a rotating drum. This type of apparatus is typically used to collect aligned structures by rotating at high speeds. However, low rotational speeds are sufficient to cause the fibers to collect flat against its surface.

Although a variety of phenomena are observed that seem somewhat random, it is important to note that the effects were readily reproducible in repeated experiments. For the various collector sizes, using the same solution, the reported morphologies repeatedly develop. It is not simply random chance that one structure will develop over the other for a given system. That is to say there are three distinct collection regimes in this study. The first is a webbed structure, the second is a webbed structure that periodically collapses inward, and the third is a centrally collecting fiber that periodically collapses outward.

Taking the decrease in collection plate size to the extreme, highly conductive fibers were also collected at the point of a copper wire. It was observed that a cotton ball like low density structure rapidly formed at the tip of the wire as shown in Figure 5-7. The fiber collected on the wire appeared to have a similar regime of thin sheets that form that regularly collapse inward.

Although the above images demonstrate a range of behaviors, a single explanation can describe the phenomena. As the conductivity of the fibers increases the fibers tend toward collecting along the electric field lines depending on the shape of the collector. For highly conductive fibers, the charges stored along their exterior are lost when one edge contacts the grounded collection plate. The fibers then remain extended outward following the electric field lines. The outward extending fibers then act as the new closest path to ground, which attracts additional fibers. However, instabilities in the electric field lead to a periodic collapse of the outward extending structures. The behavior results in a morphology that is dependent on the collector shape.

Fiber Diameter and Morphology

SEM images of fibers with varying salt concentrations collected on a circular collector of diameter 8.5 cm are shown in Figure 5-8. Even though the bulk structure of the fibers was very different, the impact on the structure of the fibers themselves appears to be limited. For the fibers spun from high salt concentrations, small particles are present on the surfaces of the fibers. These are most likely salt crystals that formed as the solvent evaporated.

Fiber diameters from 35 fibers were measured from various areas in the sample for each reported system. Figure 5-9 shows a comparison of fiber diameters. This data suggest that for each system, the as-spun fibers are approximately 200 nm. There does

not seem to be a significant effect on the diameter despite the change in shape of the macroscopic morphology.

Several other highly conductive materials were also electrospun. La doped SrTiO₃, shown in Figure 5-10, required a solution with even higher conductivity than could be achieved in the TiO₂ system. This material also formed a large low density structure. The conductivity of this system was higher than possible with the TiO₂ precursor solution. In the SrTiO₃:20% La system, the fibers had a conductivity of 3,900 μS/cm. Doubling the salt concentration in the solution increased the conductivity to 6,100 μS/cm. At this level of conductivity, the electrospinning process broke down. A few fibers formed and rapidly attached and detached from the edge of the collection plate. After 30 minutes of electrospinning, only a few fiber strands were attached to random locations in the electrospinning box instead of on the collection plate. It appears that for a given solution, there is an upper limit on the conductivity that will allow fibers to form.

The formation of low-density structures can interfere with the electrospinning process. In order to collect large quantities of nanofibers that are needed for many applications, several days may be needed to collect enough material. However, the low-density morphology can fill up the space between the collection plate and needle within hours. Once the fibers come into contact with the needle, a direct path to ground occurs, interfering with the electric field. This results in the spraying of large droplets of the precursor solution, which dissolve away the previously collected fibrous mesh. The low-density structures can be avoided altogether via a simple method of electrospinning

onto a rotating drum, as shown in Figure 5-11. The rotation of the drum forces the fibers to fall flat against the device.

Applications

There are two possible applications of the work presented here. The first involves preventing the low-density structures that form. This can be done by altering the precursor solution such that different materials or proportions of materials are used to decrease the conductivity. Alternatively, collecting fibers on a rotating drum allows collection of flat meshes. This could be useful for a range of applications that require uniform fibers. For example, filtration applications often use fiber meshes, which must be thin and uniform[179].

Conversely, low-density structures are desirable to certain applications. For example, electrospun fibers are often used as cell growth templates. Traditional fiber meshes are tightly packed, which hinders cell infiltration and growth[180]. Low-density fibrous structures allow cells to grow both on the surface and into the structure. Therefore electrospinning biocompatible polymers from high conductivity solutions could greatly improve cell growth and proliferation.

Conclusions

Precursor materials with high conductivity have important applications to energy harvesting and storage technology. Electrospun nanofibers have been applied to photocatalysts, thermoelectrics, batteries, and solar cells. These systems require complex oxide materials that tend to require precursor solutions with very high conductivities. Understanding the unusual properties of electrospinning high conductivity precursor solutions is essential to utilizing nanofibers in these systems.

In this investigation, titanium dioxide precursor solutions with conductivities above 1270 $\mu\text{S}/\text{cm}$ begin showing unusual electrospinning behavior. The fibers become concentrated along electric field lines, which are dependent on the shape of the collection plate. Rather than falling flat against the plate as in standard electrospinning conditions, the structures form three-dimensional shapes that extend outward from the collector.

The observed phenomena were dependent on the solution conductivity and shape of the collector. While the outward appearance of the fibers appeared drastically different in the various systems, there did not appear to be a significant effect on the diameter of the fibers. Although the three dimensional morphologies might appear to occur randomly, they were observed to form in a similar manner for each set of experimental conditions.

Table 5-1. Conductivity of electrospinning solutions with varying amounts of NaCl addition on a circular collection plate with a diameter of 8.5 cm.

NaCl (g)	Conductivity ($\mu\text{S}/\text{cm}$)	Morphology of fibers
0.00	153	Flat
0.01	181	Flat
0.02	744	Flat
0.03	830	Flat
0.04	1270	Webbed edges
0.05	1500	Webbed edges
0.10	2800	Fibers collect in center and collapse outward



30 minutes

Figure 5-1. 0.01g NaCl resulted in fibers collecting as a flat mesh typically observed in electrospinning. Photo credit: Michael Laudenslager.

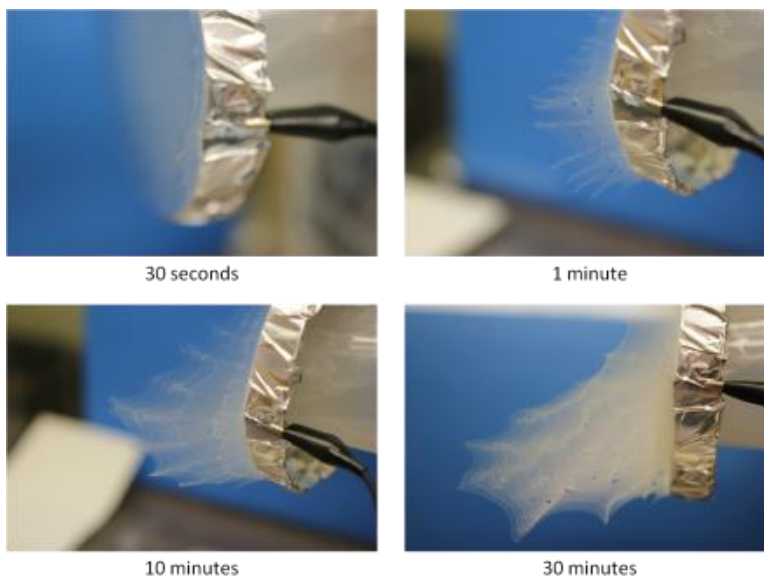


Figure 5-2. Photographs of electrospun fibers containing 0.05 g NaCl onto a collector with a diameter of 8.5 cm. The fibers collected as a webbed layer around the edges of the collection plate. Photo credit: Michael Laudenslager.

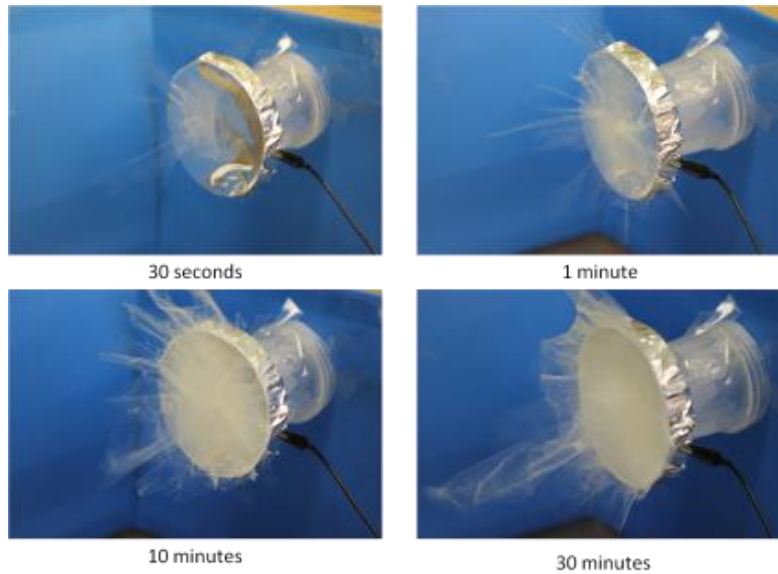


Figure 5-3. Photographs of electrospun fibers containing 0.1 g NaCl onto a collector with a diameter of 8.5 cm. The fibers collected as a webbed layer around the edges of the collection plate. Fibers collect on a centrally located strand that periodically collapses outward. When the strand collapses, a new central strand forms. Photo credit: Michael Laudenslager.



Figure 5-4. Fiber collection with 0.05 g NaCl on a collector with a diameter of 5 cm. Photo credit: Michael Laudenslager.



Figure 5-5. Conical strand of fibers extending outward from the collection plate ($d=12$ cm) towards the needle. Photo credit: Michael Laudenslager.

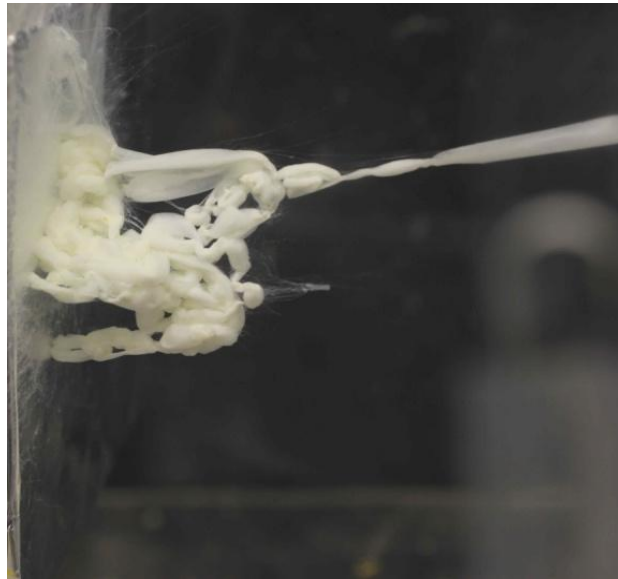


Figure 5-6. Different view of the sample in Figure 5-5 showing the looped structure that collects as the conical strand that extends to the right collapses. Photo credit: Michael Laudenslager.



Figure 5-7. Fibers collecting on a single copper wire as a low density structure for 5 minutes. Photo credit: Michael Laudenslager.

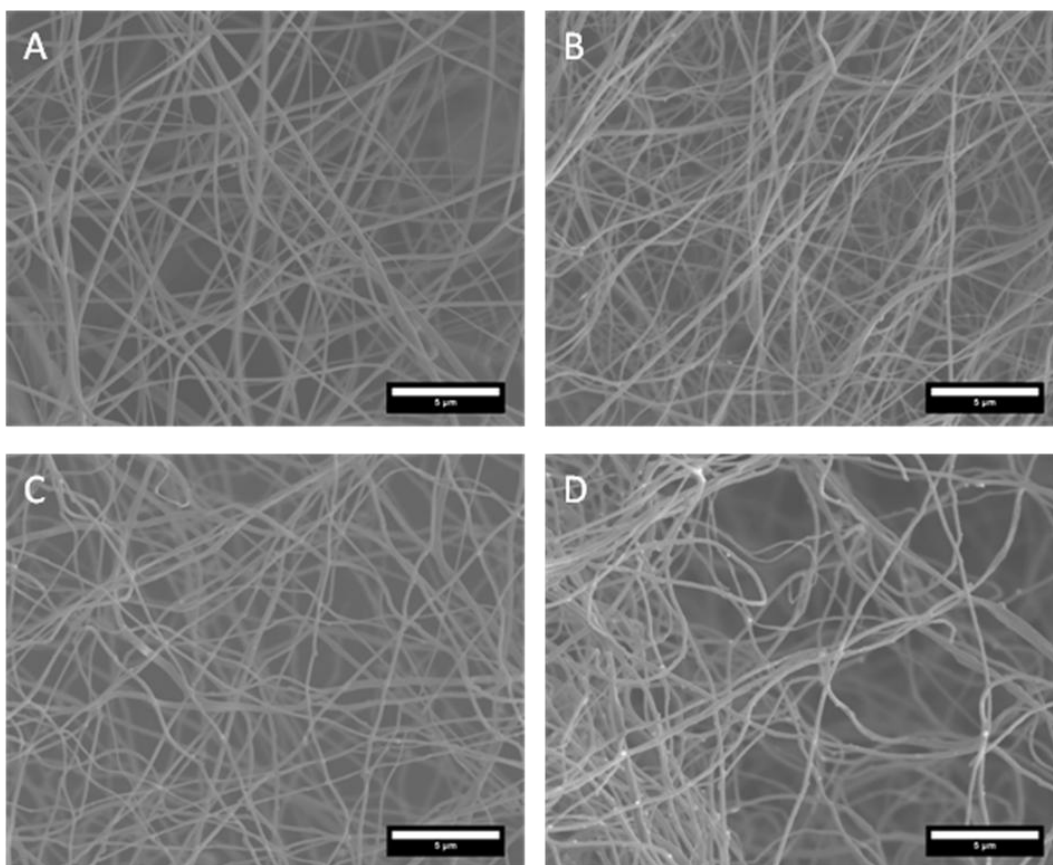


Figure 5-8. SEM images of nanofibers collected from solutions with vary conductivities. A circular collection plate with diameter of 8.5 cm was used to collect fibers

with NaCl contents of (A) 0.01 g (B) 0.05 g (C) 0.1 g. Fibers in (D) were collected on a single copper wire with a salt concentration of 0.1 g.

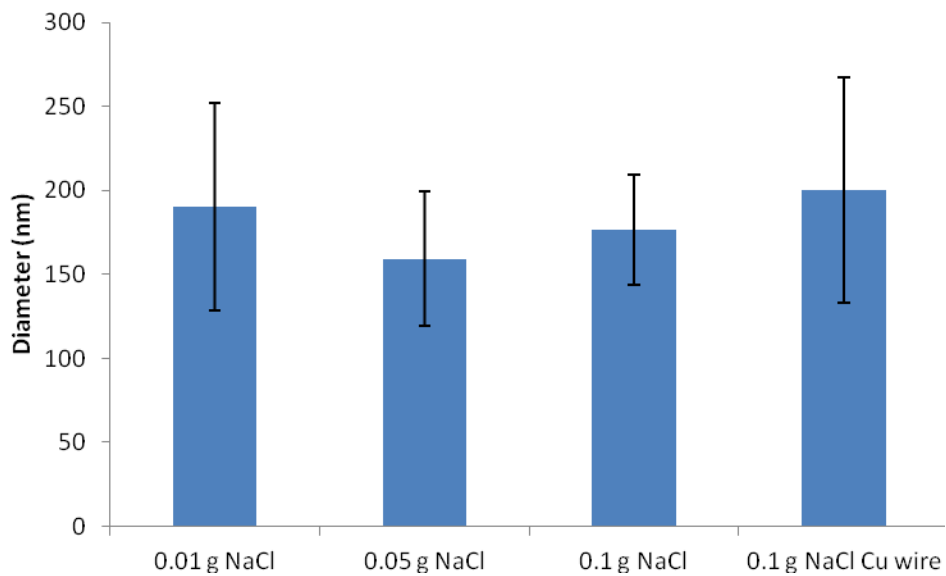


Figure 5-9. Fiber diameter at varying concentrations of NaCl on a circular collector with diameter 8.5 cm and fibers collected on a single copper wire.

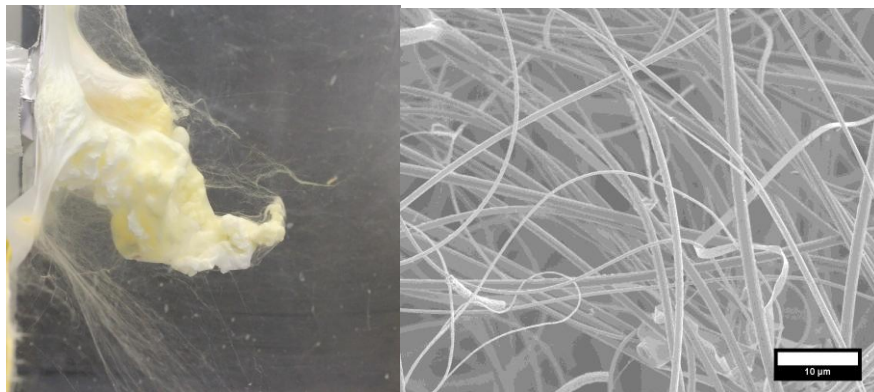


Figure 5-10. 20% La doped SrTiO₃ fibers Left: three dimensional fiber mesh spun from a solution with conductivity of 6,100 μS/cm Right: SEM images showing as-spun fibers. Photo credit: Michael Laudenslager.

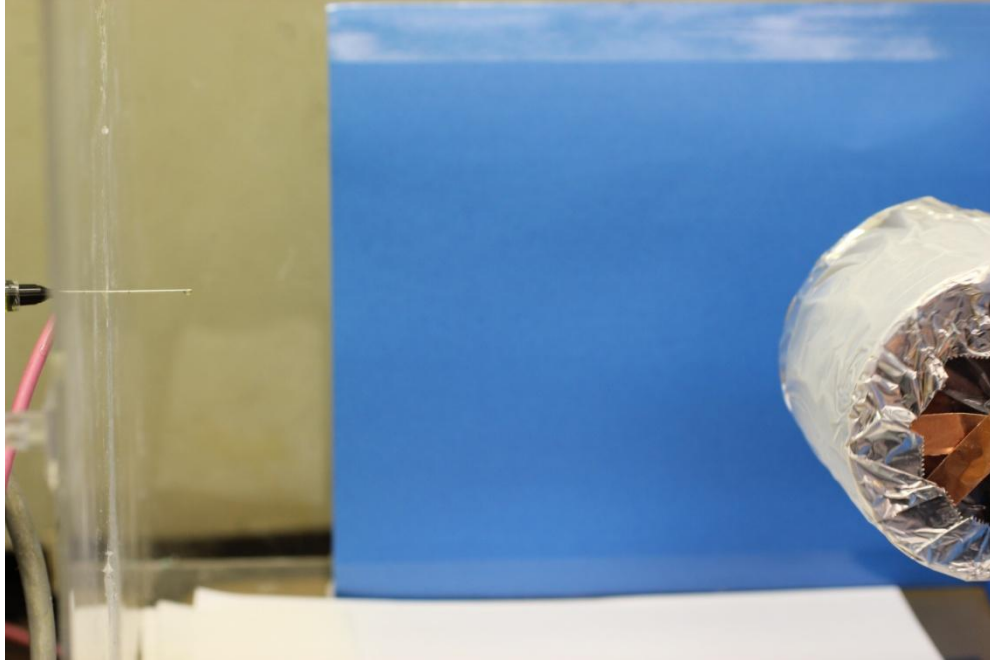


Figure 5-11. Electrospinning SrTiO_3 :20% La nanofibers onto a rotating drum prevents formation of three dimensional structures. Photo credit: Michael Laudenslager.

CHAPTER 6 CONCLUSIONS AND FUTURE WORK

Conclusions

Improving the efficiency of photocatalysts is an important area of research to maintaining clean waterways and improving overall public health. The work presented here demonstrates the ability of an electric field applied through air to enhance the reaction rate of dispersed nanoparticle systems. This method potentially allows higher electric fields to be applied without breaking down water, which is a limiting factor in other studies. The increase in performance of the P25 system was as high as 120 % with a field strength of 2,300 V/cm applied. The effect on the rate constant of an electric field of 2,300 V/cm followed the trend $P25 > SrTiO_3:20\% La > CNT/TiO_2 > rutile > ZnO/TiO_2$.

In addition, the unusual behavior observed while electrospinning photocatalytic materials was discussed. Electrospun photocatalytic materials can be used directly as supported photocatalytic systems. While pure TiO_2 electrospun nanofibers appeared relatively inactive, $SrTiO_3$ doped 20 % La fibers were found to be highly active photocatalysts. In order to electrospin the complex oxide nanofibers, a precursor solution with a high conductivity was required. The high conductivity resulted in a variety of low-density structures that developed based on the solution conductivity and shape of the electric field, which is controlled by the shape of the collection plate. This behavior has not been previously reported for electrospun systems, but has the potential to impact a large number of electrospinning applications including battery technology, thermoelectrics, and solar cells.

Future Work

Further work is needed to better understand the effects of the applied electric field on the system. Since the electric field is applied through air, the exact field strength that interacts with the particles is not known. Complex models are required to determine this data that are beyond the scope of this work. In addition, further experiments could be developed that allow a higher electric field strength to be applied to the system. The electric field enhancement effect models predict that the improvement in charge transport should level off at higher electric field strengths. The electric field effect results presented for P25 were only in the linear region of the effect. However, to further increase the electric field strength observed by the photocatalyst materials a different electric field setup would be needed. In the present system, sparking began to occur when the applied voltage was increased further, but an alternate setup might overcome this limitation.

LIST OF REFERENCES

- [1] WHO, Water-related diseases, World Health Organization, 2012.
- [2] M.R. Hoffmann, S.T. Martin, W. Choi, D.W. Bahnemann, *Chemical Reviews* 95 (1995) 69-96.
- [3] WHO, Valuing water, valuing livelihoods, World Health Organization, 2012.
- [4] J.W. Fleeger, K.R. Carman, R.M. Nisbet, *Science of the Total Environment* 317 (2003) 207-233.
- [5] K. Kabra, R. Chaudhary, R.L. Sawhney, *Industrial & Engineering Chemistry Research* 43 (2004) 7683-7696.
- [6] C. Galindo, P. Jacques, A. Kalt, *Chemosphere* 45 (2001) 997-1005.
- [7] Z. Huang, P.-C. Maness, D.M. Blake, E.J. Wolfrum, S.L. Smolinski, W.A. Jacoby, *Journal of Photochemistry and Photobiology A: Chemistry* 130 (2000) 163-170.
- [8] U. Diebold, *Nature Chemistry* 3 (2011) 271-272.
- [9] K. Hashimoto, H. Irie, A. Fujishima, *JAPANESE JOURNAL OF APPLIED PHYSICS PART 1 REGULAR PAPERS SHORT NOTES AND REVIEW PAPERS* 44 (2005) 8269.
- [10] M.A. Henderson, *Surface Science Reports* 66 (2011) 185-297.
- [11] J. Nowotny, T. Bak, M.K. Nowotny, L.R. Sheppard, *The Journal of Physical Chemistry B* 110 (2006) 18492-18495.
- [12] J. Peral, X. Domènech, D.F. Ollis, *Journal of chemical technology and biotechnology* 70 (1997) 117-140.
- [13] R.I. Bickley, T. Gonzalez-Carreno, J.S. Lees, L. Palmisano, R.J.D. Tilley, *Journal of Solid State Chemistry* 92 (1991) 178-190.
- [14] A.K. Datye, G. Riegel, J.R. Bolton, M. Huang, M.R. Prairie, *Journal of Solid State Chemistry* 115 (1995) 236-239.
- [15] T. Ohno, K. Sarukawa, K. Tokieda, M. Matsumura, *Journal of Catalysis* 203 (2001) 82-86.
- [16] J. Liqiang, S. Xiaojun, S. Jing, C. Weimin, X. Zili, D. Yaoguo, F. Honggang, *Solar Energy Materials and Solar Cells* 79 (2003) 133-151.

- [17] E. Wahlström, E.K. Vestergaard, R. Schaub, A. Rønnau, M. Vestergaard, E. Lægsgaard, I. Stensgaard, F. Besenbacher, *Science* 303 (2004) 511-513.
- [18] A. Furube, T. Asahi, H. Masuhara, H. Yamashita, M. Anpo, *The Journal of Physical Chemistry B* 103 (1999) 3120-3127.
- [19] U. Diebold, *Surface Science Reports* 48 (2003) 53-229.
- [20] F. Zuo, L. Wang, T. Wu, Z. Zhang, D. Borchardt, P. Feng, *Journal of the American Chemical Society* 132 (2010) 11856-11857.
- [21] R.D. Shannon, *Journal of Applied Physics* 35 (1964) 3414-3416.
- [22] X. Chen, L. Liu, P.Y. Yu, S.S. Mao, *Science* 331 (2011) 746.
- [23] D.C. Hurum, A.G. Agrios, K.A. Gray, T. Rajh, M.C. Thurnauer, *The Journal of Physical Chemistry B* 107 (2003) 4545-4549.
- [24] T. Ohno, K. Sarukawa, M. Matsumura, *The Journal of Physical Chemistry B* 105 (2001) 2417-2420.
- [25] G. Riegel, J.R. Bolton, *The Journal of Physical Chemistry* 99 (1995) 4215-4224.
- [26] G. Xiang, Y.G. Wang, D. Wu, T. Li, J. He, J. Li, X. Wang, *Chemistry-A European Journal* (2012).
- [27] R. Su, R. Bechstein, L. Sør, R.T. Vang, M. Sillassen, B. Esbjörnsson, A. Palmqvist, F. Besenbacher, *The Journal of Physical Chemistry C* 115 (2011) 24287-24292.
- [28] B. Ohtani, Y. Okugawa, S. Nishimoto, T. Kagiya, *Journal of Physical Chemistry* 91 (1987) 3550-3555.
- [29] L. Jing, S. Li, S. Song, L. Xue, H. Fu, *Solar Energy Materials and Solar Cells* 92 (2008) 1030-1036.
- [30] X. Zhang, Y. Lin, D. He, J. Zhang, Z. Fan, T. Xie, *Chemical Physics Letters* 504 (2011) 71-75.
- [31] B. Sun, A.V. Vorontsov, P.G. Smirniotis, *Langmuir* 19 (2003) 3151-3156.
- [32] J. Nowotny, M. RADECKA, M. REKAS, *Journal of Physics and Chemistry of Solids* 58 (1997) 927-937.
- [33] N.A. Deskins, M. Dupuis, *Physical Review B* 75 (2007) 195212.

- [34] E. Hendry, M. Koeberg, B. O'Regan, M. Bonn, Nano letters 6 (2006) 755-759.
- [35] I. Butterfield, P. Christensen, A. Hamnett, K. Shaw, G. Walker, S. Walker, C. Howarth, Journal of applied electrochemistry 27 (1997) 385-395.
- [36] J. Yu, J. Fan, K. Lv, Nanoscale 2 (2010) 2144-2149.
- [37] X. Han, Q. Kuang, M. Jin, Z. Xie, L. Zheng, Journal of the American Chemical Society 131 (2009) 3152-3153.
- [38] H.G. Yang, C.H. Sun, S.Z. Qiao, J. Zou, G. Liu, S.C. Smith, H.M. Cheng, G.Q. Lu, Nature 453 (2008) 638-641.
- [39] M. Lazzeri, A. Vittadini, A. Selloni, Physical Review B 65 (2002) 119901.
- [40] T. Ohno, K. Sarukawa, M. Matsumura, New Journal of Chemistry 26 (2002) 1167-1170.
- [41] S. Liu, E. Guo, L. Yin, J. Mater. Chem. (2012).
- [42] I. Justicia, P. Ordejón, G. Canto, J. Mozos, J. Fraxedas, G. Battiston, R. Gerbasi, A. Figueras, Phys. Lett 74 (1999) 3824.
- [43] F. Dong, W. Zhao, Z. Wu, S. Guo, Journal of Hazardous Materials 162 (2009) 763-770.
- [44] M. Ni, M.K.H. Leung, D.Y.C. Leung, K. Sumathy, Renewable and Sustainable Energy Reviews 11 (2007) 401-425.
- [45] C. Di Valentin, G. Pacchioni, A. Selloni, Chemistry of Materials 17 (2005) 6656-6665.
- [46] D.B. Warheit, R.A. Hoke, C. Finlay, E.M. Donner, K.L. Reed, C.M. Sayes, Toxicology letters 171 (2007) 99-110.
- [47] M. Tomkiewicz, Catalysis Today 58 (2000) 115-123.
- [48] N.J. Peill, M.R. Hoffmann, Environmental Science & Technology 29 (1995) 2974-2981.
- [49] G. Li Puma, A. Bono, D. Krishnaiah, J.G. Collin, Journal of Hazardous Materials 157 (2008) 209-219.
- [50] H. Uchida, S. Itoh, H. Yoneyama, Chemistry letters 22 (1993) 1995-1998.
- [51] J.S. Im, M.I. Kim, Y.S. Lee, Materials Letters 62 (2008) 3652-3655.

- [52] T. He, Z. Zhou, W. Xu, F. Ren, H. Ma, J. Wang, *Polymer* 50 (2009) 3031-3036.
- [53] Z. Zhang, C. Shao, X. Li, L. Zhang, H. Xue, C. Wang, Y. Liu, *The Journal of Physical Chemistry C* 114 (2010) 7920-7925.
- [54] Y. Yang, H. Wang, X. Li, C. Wang, *Materials Letters* 63 (2009) 331-333.
- [55] S.-w. Lee, J. Drwiega, C.-Y. Wu, D. Mazyck, W.M. Sigmund, *Chemistry of Materials* 16 (2004) 1160-1164.
- [56] S. Watson, D. Beydoun, R. Amal, *Journal of Photochemistry and Photobiology A: Chemistry* 148 (2002) 303-313.
- [57] M.-W. Xu, S.-J. Bao, X.-G. Zhang, *Materials Letters* 59 (2005) 2194-2198.
- [58] L. Zhang, W. Wang, L. Zhou, M. Shang, S. Sun, *Applied Catalysis B: Environmental* 90 (2009) 458-462.
- [59] J. Porter, Washington, DC (1973).
- [60] Y. Liu, J. Dadap, D. Zimdars, K.B. Eisenthal, *The Journal of Physical Chemistry B* 103 (1999) 2480-2486.
- [61] K. Vinodgopal, D.E. Wynkoop, P.V. Kamat, *Environmental Science & Technology* 30 (1996) 1660-1666.
- [62] M. Muneer, R. Philip, S. Das, *Research on chemical intermediates* 23 (1997) 233-246.
- [63] C. Bauer, P. Jacques, A. Kalt, *Journal of Photochemistry and Photobiology A: Chemistry* 140 (2001) 87-92.
- [64] C.M. So, M.Y. Cheng, J.C. Yu, P.K. Wong, *Chemosphere* 46 (2002) 905-912.
- [65] D. Vasudevan, A.T. Stone, *Environmental Science & Technology* 30 (1996) 1604-1613.
- [66] H. Chun, W. Yizhong, T. Hongxiao, *Applied Catalysis B: Environmental* 35 (2001) 95-105.
- [67] S. Tunesi, M.A. Anderson, *Langmuir* 8 (1992) 487-495.
- [68] R.R. Bacsa, J. Kiwi, *Applied Catalysis B: Environmental* 16 (1998) 19-29.
- [69] M. Kosmulski, *Advances in Colloid and Interface Science* 99 (2002) 255-264.

- [70] U.G. Akpan, B.H. Hameed, *Journal of Hazardous Materials* 170 (2009) 520-529.
- [71] C. So, M.Y. Cheng, J. Yu, P. Wong, *Chemosphere* 46 (2002) 905-912.
- [72] J.M. Joseph, H. Destailats, H.M. Hung, M.R. Hoffmann, *The Journal of Physical Chemistry A* 104 (2000) 301-307.
- [73] C. Hu, J.C. Yu, Z. Hao, P.K. Wong, *Applied Catalysis B: Environmental* 42 (2003) 47-55.
- [74] H. Lachheb, E. Puzenat, A. Houas, M. Ksibi, E. Elaloui, C. Guillard, J.M. Herrmann, *Applied Catalysis B: Environmental* 39 (2002) 75-90.
- [75] G. Sivalingam, K. Nagaveni, M. Hegde, G. Madras, *Applied Catalysis B: Environmental* 45 (2003) 23-38.
- [76] I.K. Konstantinou, T.A. Albanis, *Applied Catalysis B: Environmental* 49 (2004) 1-14.
- [77] D.S. Bhatkhande, V.G. Pangarkar, A.A. Beenackers, *Journal of chemical technology and biotechnology* 77 (2002) 102-116.
- [78] U.I. Gaya, A.H. Abdullah, *Journal of Photochemistry and Photobiology C: Photochemistry Reviews* 9 (2008) 1-12.
- [79] I.K. Konstantinou, T.A. Albanis, *Applied Catalysis B: Environmental* 49 (2004) 1-14.
- [80] C. Guillard, H. Lachheb, A. Houas, M. Ksibi, E. Elaloui, J.M. Herrmann, *Journal of Photochemistry and Photobiology A: Chemistry* 158 (2003) 27-36.
- [81] A.A. Gribb, J.F. Banfield, *American Mineralogist* 82 (1997) 717-728.
- [82] J. Ananpattarachai, P. Kajitvichyanukul, S. Seraphin, *Journal of Hazardous Materials* 168 (2009) 253-261.
- [83] G.T. Brown, J.R. Darwent, *J. Chem. Soc., Chem. Commun.* (1985) 98-100.
- [84] H.-S. Lee, T. Hur, S. Kim, J.-H. Kim, H.-I. Lee, *Catalysis Today* 84 (2003) 173-180.
- [85] C. Itoh, K. Iwahashi, K.-i. Kan'no, *Nuclear Instruments and Methods in Physics Research Section B: Beam Interactions with Materials and Atoms* 191 (2002) 271-274.
- [86] Z. Jiang, H. Wang, H. Huang, C. Cao, *Chemosphere* 56 (2004) 503-508.

- [87] K. Woan, G. Pyrgiotakis, W. Sigmund, *Advanced Functional Materials* 18 (2009) 23.
- [88] T. Lana-Villarreal, J. Bisquert, I. Mora-Seró, P. Salvador, *The Journal of Physical Chemistry B* 109 (2005) 10355-10361.
- [89] J. Nowotny, *Oxide Semiconductors for Solar Energy Conversion Titanium Dioxide*, CRC Press, Boca Raton, 2011.
- [90] H. Seo, M.-K. Son, I. Shin, J.-K. Kim, K.-J. Lee, K. Prabakar, H.-J. Kim, *Electrochimica Acta* 55 (2010) 4120-4123.
- [91] M. Soliman Selim, R. Seoudi, A.A. Shabaka, *Materials Letters* 59 (2005) 2650-2654.
- [92] C.C. Ho, R.H. Ottewill, L. Yu, *Langmuir* 13 (1997) 1925-1930.
- [93] V.N. Shilov, A.V. Delgado, F. González-Caballero, J. Horno, G. López, amp, x, J.J. a, C. Grosse, *Journal of Colloid and Interface Science* 232 (2000) 141-148.
- [94] J.L. Anderson, *Journal of Colloid and Interface Science* 105 (1985) 45-54.
- [95] D. Saintillan, E. Darve, E.S.G. Shaqfeh, *Journal of Fluid Mechanics* 563 (2006) 223-259.
- [96] L. Marshall, C.F. Zukoski, J.W. Goodwin, *Journal of the Chemical Society, Faraday Transactions 1: Physical Chemistry in Condensed Phases* 85 (1989) 2785-2795.
- [97] M.S. Wrighton, D.S. Ginley, P.T. Wolczanski, A.B. Ellis, D.L. Morse, A. Linz, *Proceedings of the National Academy of Sciences* 72 (1975) 1518-1522.
- [98] G. Li, J. Qu, X. Zhang, J. Ge, *Water Research* 40 (2006) 213-220.
- [99] N.A. Deskins, R. Rousseau, M. Dupuis, *The Journal of Physical Chemistry C* 113 (2009) 14583-14586.
- [100] S.-G. Chen, P. Stradins, B.A. Gregg, *The Journal of Physical Chemistry B* 109 (2005) 13451-13460.
- [101] J. Mort, *Physical Review B* 5 (1972) 3329.
- [102] B. Lalevic, G. Taylor, *Journal of Applied Physics* 46 (1975) 3208-3210.
- [103] V. Coropceanu, J. Cornil, D.A. da Silva Filho, Y. Olivier, R. Silbey, J.-L. Brédas, *Chemical Reviews* 107 (2007) 926-952.

- [104] W. Gill, *Journal of Applied Physics* 43 (1972) 5033-5040.
- [105] M.K. Nowotny, T. Bak, J. Nowotny, *The Journal of Physical Chemistry B* 110 (2006) 16270-16282.
- [106] L. Mai, C. Han, *Materials Letters* 62 (2008) 1458-1461.
- [107] M. Feng, M. Zhang, J.-M. Song, X.-G. Li, S.-H. Yu, *ACS Nano* 5 (2011) 6726-6735.
- [108] M.J. Hanna, H. Zhao, J.C. Lee, *Applied Physics Letters* 101 (2012) 153504-153504-153504.
- [109] R.A. Marsh, J.M. Hodgkiss, R.H. Friend, *Advanced Materials* 22 (2010) 3672-3676.
- [110] M. Royo, J.I. Climente, J.L. Movilla, J. Planelles, *Journal of Physics: Condensed Matter* 23 (2011) 015301.
- [111] I. Butterfield, P. Christensen, T. Curtis, J. Gunlazuardi, *Water Research* 31 (1997) 675-677.
- [112] M.S. White, D.C. Olson, N. Kopidakis, A.M. Nardes, D.S. Ginley, J.J. Berry, *physica status solidi (a)* 207 (2010) 1257-1265.
- [113] L. Hench, J. West, *Chem. Rev* 90 (1990) 33-72.
- [114] C. Sanchez, J. Livage, M. Henry, F. Babonneau, *Journal of Non-Crystalline Solids* 100 (1988) 65-76.
- [115] S. Doeuff, M. Henry, C. Sanchez, J. Livage, *Journal of Non-Crystalline Solids* 89 (1987) 206-216.
- [116] V.G. Kessler, G.I. Spijksma, G.A. Seisenbaeva, S. Håkansson, D.H.A. Blank, H.J.M. Bouwmeester, *Journal of sol-gel science and technology* 40 (2006) 163-179.
- [117] A. Greiner, J. Wendorff, *Angewandte Chemie International Edition* 46 (2007) 5670-5703.
- [118] A. Greiner, J. Wendorff, *Self-Assembled Nanomaterials I* (2008) 107-171.
- [119] Z. Huang, Y. Zhang, M. Kotaki, S. Ramakrishna, *Composites Science and Technology* 63 (2003) 2223-2253.

- [120] R. Ramaseshan, S. Sundarrajan, R. Jose, S. Ramakrishna, *Journal of Applied Physics* 102 (2007) 111101.
- [121] W. Sigmund, J. Yuh, H. Park, V. Maneeratana, G. Pyrgiotakis, A. Daga, J. Taylor, J. Nino, *Journal of the American Ceramic Society* 89 (2006) 395-407.
- [122] S. Tan, X. Huang, B. Wu, *Polymer International* 56 (2007) 1330-1339.
- [123] G. Rutledge, S. Fridrikh, *Advanced drug delivery reviews* 59 (2007) 1384-1391.
- [124] A. Yarin, S. Koombhongse, D. Reneker, *Journal of Applied Physics* 90 (2001) 4836.
- [125] M. Hohman, M. Shin, G. Rutledge, M. Brenner, *Physics of fluids* 13 (2001) 2201.
- [126] W. Gilbert, P. Mottelay, *De magnete*, Dover Pubns, 1958.
- [127] L. Rayleigh, *Phil. Mag* 14 (1882) 184.
- [128] G. Taylor, *Proceedings of the Royal Society of London. Series A, Mathematical and Physical Sciences* (1964) 383-397.
- [129] M.J. Laudenslager, W.M. Sigmund, *American Ceramic Society Bulletin* 90 (2011) 22-26.
- [130] J. Cooley, *Apparatus for electrically dispersing fluids* Feb. 4th, 1902.
- [131] W. Morton, *Method of dispersing fluids* Issued July 29th, 1902.
- [132] A. Formhals, *Process and apparatus for preparing artificial threads*, US Patent 1,975,504, Issued Oct. 2nd 1934.
- [133] H. Dai, J. Gong, H. Kim, D. Lee, *Nanotechnology* 13 (2002) 674.
- [134] M. Laudenslager, R. Scheffler, W. Sigmund, *Pure Appl. Chem.* 82 (2010) 2137-2156.
- [135] S. Fridrikh, J. Yu, M. Brenner, G. Rutledge, *Physical Review Letters* 90 (2003) 144502-144502.
- [136] M. Wang, H. Singh, T. Hatton, G. Rutledge, *Polymer* 45 (2004) 5505-5514.
- [137] N. Dharmaraj, H. Park, C. Kim, H. Kim, D. Lee, *Materials Chemistry and Physics* 87 (2004) 5-9.

- [138] H. Guan, C. Shao, S. Wen, B. Chen, J. Gong, X. Yang, *Materials Chemistry and Physics* 82 (2003) 1002-1006.
- [139] C. Shao, H. Guan, Y. Liu, X. Li, X. Yang, *Journal of Solid State Chemistry* 177 (2004) 2628-2631.
- [140] X. Yang, C. Shao, Y. Liu, R. Mu, H. Guan, *Thin Solid Films* 478 (2005) 228-231.
- [141] Y. Gu, F. Jian, *The Journal of Physical Chemistry C* 112 (2008) 20176-20180.
- [142] Z. Sun, E. Zussman, A. Yarin, J. Wendorff, A. Greiner, *Advanced Materials* 15 (2003) 1929-1932.
- [143] I. Loscertales, A. Barrero, M. Márquez, R. Spretz, R. Velarde-Ortiz, G. Larsen, *J. Am. Chem. Soc* 126 (2004) 5376-5377.
- [144] D. Li, Y. Xia, *Nano Letters* 4 (2004) 933-938.
- [145] A. Baji, Y.-W. Mai, S.-C. Wong, M. Abtahi, P. Chen, *Composites Science and Technology* 70 (2010) 703-718.
- [146] X. Cui, L. Li, J. Xu, F. Xu, *Journal of Applied Polymer Science* 116 (2010) 3676-3681.
- [147] P.D. Dalton, D. Klee, M. Möller, *Polymer* 46 (2005) 611-614.
- [148] J. Deitzel, J. Kleinmeyer, J. Hirvonen, N. Beck Tan, *Polymer* 42 (2001) 8163-8170.
- [149] P. Katta, M. Alessandro, R. Ramsier, G. Chase, *Nano letters* 4 (2004) 2215-2218.
- [150] M. Khamforoush, M. Mahjob, *Materials Letters* 65 (2011) 453-455.
- [151] D. Li, Y. Wang, Y. Xia, *Nano Letters* 3 (2003) 1167-1171.
- [152] D. Li, Y. Wang, Y. Xia, *Advanced Materials* 16 (2004) 361-366.
- [153] H. Pan, L. Li, L. Hu, X. Cui, *Polymer* 47 (2006) 4901-4904.
- [154] V. Secasanu, C. Giardina, Y. Wang, *Biotechnology progress* 25 (2009) 1169-1175.
- [155] A. Subramanian, U.M. Krishnan, S. Sethuraman, *Biomedical Materials* 6 (2011) 025004.

- [156] B. Sundaray, V. Subramanian, T. Natarajan, R. Xiang, C. Chang, W. Fann, *Applied Physics Letters* 84 (2004) 1222.
- [157] W. Teo, M. Kotaki, X. Mo, S. Ramakrishna, *Nanotechnology* 16 (2005) 918-924.
- [158] W. Teo, S. Ramakrishna, *Nanotechnology* 16 (2005) 1878-1884.
- [159] W. Teo, S. Ramakrishna, *Nanotechnology* 17 (2006) 89.
- [160] A. Theron, E. Zussman, A. Yarin, *Nanotechnology* 12 (2001) 384-390.
- [161] G. Wnek, M. Carr, D. Simpson, G. Bowlin, *Nano letters* 3 (2003) 213-216.
- [162] H. Wu, D. Lin, R. Zhang, W. Pan, *Journal of the American Ceramic Society* 90 (2007) 632-634.
- [163] J. Xie, M.R. MacEwan, W.Z. Ray, W. Liu, D.Y. Siewe, Y. Xia, *ACS Nano* 4 (2010) 5027-5036
- [164] C.Y. Xu, R. Inai, M. Kotaki, S. Ramakrishna, *Biomaterials* 25 (2004) 877-886.
- [165] E. Zussman, A. Theron, A. Yarin, *Applied Physics Letters* 82 (2003) 973.
- [166] J. Matthews, G. Wnek, D. Simpson, G. Bowlin, *Biomacromolecules* 3 (2002) 232-238.
- [167] H. Fong, I. Chun, D.H. Reneker, *Polymer* 40 (1999) 4585-4592.
- [168] K. Acatay, E. Simsek, C. Ow Yang, Y.Z. Menceloglu, *Angewandte Chemie International Edition* 43 (2004) 5210-5213.
- [169] D.H. Reneker, A.L. Yarin, *Polymer* 49 (2008) 2387-2425.
- [170] Q. Yu, M. Wang, H. Chen, *Materials Letters* 64 (2010) 428-430.
- [171] D.L. Liao, C.A. Badour, B.Q. Liao, *Journal of Photochemistry and Photobiology A: Chemistry* 194 (2008) 11-19.
- [172] R.A. Spurr, H. Myers, *Analytical Chemistry* 29 (1957) 760-762.
- [173] K. Szot, W. Speier, J. Herion, C. Freiburg, *Applied Physics A: Materials Science & Processing* 64 (1996) 55-59.
- [174] G. Pyrgiotakis, *Titania carbon nanotube composites for enhanced photocatalysis*, *Materials Science and Engineering*, University of Florida, Gainesville, 2006.

- [175] B. Misch, A. Firus, G. Brunner, *The Journal of Supercritical Fluids* 17 (2000) 227-237.
- [176] H. Hosono, *Nature* 1 (2010).
- [177] G. Xu, H. Liang, *Journal of electronic materials* 31 (2002) 272-277.
- [178] C. Zhang, X. Yuan, L. Wu, Y. Han, J. Sheng, *European Polymer Journal* 41 (2005) 423-432.
- [179] Q. Zhang, J. Welch, H. Park, C.-Y. Wu, W. Sigmund, J.C.M. Marijnissen, *Journal of aerosol science* 41 (2010) 230-236.
- [180] B.A. Blakeney, A. Tambralli, J.M. Anderson, A. Andukuri, D.J. Lim, D.R. Dean, H.W. Jun, *Biomaterials* 32 (2011) 1583-1590.

BIOGRAPHICAL SKETCH

In 2008, Michael Laudenslager completed a combined bachelor's and master's degree program in materials engineering from Drexel University. During his master's research, Michael worked with Dr. Caroline Schauer on polymer catalyst supports. Upon graduation, Michael continued with his study of materials engineering at the University of Florida. There, his research focused on electrospinning, sol-gel processing, and photocatalysis. Michael was awarded a National Science Foundation East Asia and Pacific Summer Institutes Program to conduct research in S. Korea at Hanyang University. He also received funding from the UF Alumni Fellowship as well as the Sandia Excellence Program.